Monthly Notices of the ROYAL ASTRONOMICAL SOCIETY

MNRAS **444,** 3926–3947 (2014) doi:10.1093/mnras/stu1615

The 6dF Galaxy Survey: cosmological constraints from the velocity power spectrum

Andrew Johnson,[1,2]★ Chris Blake,[1] Jun Koda,[1,2] Yin-Zhe Ma,[3,4] Matthew Colless,[5] Martin Crocce,[6] Tamara M. Davis,[7] Heath Jones,[8,9] Christina Magoulas,[9,10,11] John R. Lucey,[12] Jeremy Mould,[1] Morag I. Scrimgeour[13,14] and Christopher M. Springob[2,9,15]

Affiliations are listed at the end of the paper

Accepted 2014 August 7. Received 2014 July 15; in original form 2014 March 6

ABSTRACT

We present scale-dependent measurements of the normalized growth rate of structure $f\sigma_8(k, z = 0)$ using only the peculiar motions of galaxies. We use data from the 6-degree Field Galaxy Survey velocity sample together with a newly compiled sample of low-redshift ($z < 0.07$) Type Ia supernovae. We constrain the growth rate in a series of $\Delta k \sim 0.03\,h\,\mathrm{Mpc}^{-1}$ bins to ∼35 per cent precision, including a measurement on scales $>300\,h^{-1}$ Mpc, which represents one of the largest scale growth rate measurement to date. We find no evidence for a scale-dependence in the growth rate, or any statistically significant variation from the growth rate as predicted by the *Planck* cosmology. Bringing all the scales together, we determine the normalized growth rate at $z = 0$ to ∼15 per cent in a manner *independent* of galaxy bias and in excellent agreement with the constraint from the measurements of redshift-space distortions from 6-degree Field Galaxy Survey. We pay particular attention to systematic errors. We point out that the intrinsic scatter present in Fundamental Plane and Tully–Fisher relations is only Gaussian in logarithmic distance units; wrongly assuming it is Gaussian in linear (velocity) units can bias cosmological constraints. We also analytically marginalize over zero-point errors in distance indicators, validate the accuracy of all our constraints using numerical simulations, and demonstrate how to combine different (correlated) velocity surveys using a matrix 'hyperparameter' analysis. Current and forthcoming peculiar velocity surveys will allow us to understand in detail the growth of structure in the low-redshift universe, providing strong constraints on the nature of dark energy.

Key words: surveys – cosmological parameters – cosmology: observations – dark energy – large-scale structure of Universe.

1 INTRODUCTION

A flat universe evolved according to the laws of General Relativity (GR), including a cosmological constant Λ and structure seeded by nearly scale-invariant Gaussian fluctuations, currently provides an excellent fit to a range of observations: cosmic microwave background (CMB) data (Planck Collaboration XVI 2013), baryon acoustic oscillations (Blake et al. 2011b; Anderson et al. 2013), supernova (SN) observations (Conley et al. 2011; Freedman et al. 2012; Ganeshalingam, Li & Filippenko 2013), and redshift-space distortion (RSD) measurements (Blake et al. 2011a; Reid et al. 2012). While the introduction of a cosmological constant term allows observational concordance by inducing a late-time period of accelerated expansion, its physical origin is currently unknown. The inability to explain the origin of this energy density component strongly suggests that our current understanding of gravitation and particle physics, the foundations of the standard model of cosmology, may be significantly incomplete. Various mechanisms extending the standard model have been suggested to explain this acceleration period such as modifying the Einstein–Hilbert action by e.g. considering a generalized function of the Ricci scalar (Sotiriou & Faraoni 2010), introducing additional matter components such as quintessence models, and investigating the influence structure has on the large-scale evolution of the universe (Clifton 2013; Wiltshire 2013).

Inhomogeneous structures in the late-time universe source gravitational potential wells that induce 'peculiar velocities' (PVs) of

★E-mail: asjohnson@swin.edu.au

galaxies, i.e. the velocity of a galaxy relative to the Hubble rest frame. The quantity we measure is the line-of-sight PV, as this component produces Doppler distortions in the observed redshift. Determination of the line-of-sight motion of galaxies requires a redshift-independent distance estimate. Such estimates can be performed using empirical relationships between galaxy properties such as the 'Fundamental Plane' (FP) or 'Tully–Fisher' relation, or one can use 'standard candles' such as Type Ia SNe (Colless et al. 2001; Springob et al. 2007; Magoulas et al. 2010; Turnbull et al. 2012). A key benefit of directly analysing PV surveys is that their interpretation is independent of the relation between galaxies and the underlying matter distribution, known as 'galaxy bias' (Cole & Kaiser 1989). The standard assumptions for galaxy bias are that it is local, linear, and deterministic (Fry & Gaztanaga 1993); such assumptions may break down on small scales and introduce systematic errors in the measurement of cosmological parameters (e.g. Cresswell & Percival 2009). Similar issues may arise when inferring the matter velocity field from the galaxy velocity field: the galaxy velocity field may not move coherently with the matter distribution, generating a 'velocity bias'. However, such an effect is negligible given current statistical errors (Desjacques et al. 2010).

Recent interest in PV surveys has been driven by the results of Watkins, Feldman & Hudson (2009), which suggest that the local 'bulk flow' (i.e. the dipole moment) of the PV field is inconsistent with the predictions of the standard Λ cold dark matter (ΛCDM) model; other studies have revealed a bulk flow more consistent with the standard model (Ma & Scott 2013). PV studies were a very active field of cosmology in the 1990s as reviewed by Strauss & Willick (1995) and Kaiser (1988). Separate from the measurement of the bulk flow of local galaxies, a number of previous studies have focused on extracting a measurement of the matter power spectrum in k-dependent bins (e.g. see Jaffe & Kaiser 1995; Freudling et al. 1999; Zehavi & Dekel 2000; Silberman et al. 2001; Zaroubi et al. 2001; Macaulay et al. 2012). This quantity is closely related to the velocity power spectrum. Other studies have focused on directly constraining standard cosmological parameters (Gordon, Land & Slosar 2007; Abate & Erdoğdu 2009).

The quantity we can directly measure from the 2-point statistics of PV surveys is the velocity divergence power spectrum.[1] The amplitude of the velocity divergence power spectrum depends on the rate at which structure grows and can therefore be used to test modified gravity models, which have been shown to cause prominent distortions in this measure relative to the matter power spectrum (Jennings et al. 2012). In addition, by measuring the velocity power spectrum we are able to place constraints on cosmological parameters such as σ_8 and $\Omega_{\rm m}$ (the rms of density fluctuations, at linear order, in spheres of comoving radius $8\,h^{-1}$ Mpc; and the fractional matter density at $z = 0$, respectively). Such constraints provide an interesting consistency check of the standard model, as the constraint on σ_8 measured from the CMB requires extrapolation from the very high redshift universe.

The growth rate of structure $f(k, a)$ describes the rate at which density perturbations grow by gravitational amplification. It is generically a function of the cosmic scalefactor a, the comoving wavenumber k and the growth factor $D(k, a)$; expressed as $f(k, a) \equiv {\rm d}\ln D(k, a)/{\rm d}\ln a$. We define $\delta(k, a) \equiv \rho(k, a)/\bar{\rho}(a) - 1$, as the fractional matter overdensity and $D(k, a) \equiv \delta(k, a)/\delta(k, a = 1)$.

The temporal dependence of the growth rate has been readily measured (up to $z \sim 0.9$) by galaxy surveys using RSD measurements (Blake et al. 2011a; Beutler et al. 2013b; de la Torre et al. 2013), while the spatial dependence is currently only weakly constrained,[2] particularly on large spatial scales (Bean & Tangmatitham 2010; Daniel & Linder 2013). The observations are in fact sensitive to the 'normalized growth rate' $f(k, z)\sigma_8(z)$, which we will write as $f\sigma_8(k, z) \equiv f(k, z)\sigma_8(z)$. Recent interest in the measurement of the growth rate has been driven by the lack of constraining power of geometric probes on modified gravity models, which can generically reproduce a given expansion history (given extra degrees of freedom). Therefore, by combining measurements of geometric and dynamical probes strong constraints can be placed on modified gravity models (Linder 2005).

A characteristic prediction of GR is a scale-independent growth rate, while modified gravity models commonly induce a scale-dependence in the growth rate. For $f(R)$ theories of gravity this transition regime is determined by the Compton wavelength scale of the extra scalar degree of freedom (for recent reviews of modified gravity models see Tsujikawa 2010; Clifton et al. 2012). Furthermore, clustering of the dark energy can introduce a scale-dependence in the growth rate (Parfrey et al. 2011). Such properties arise in scalar field models of dark energy such as quintessence and k-essence (Caldwell, Dave & Steinhardt 1998; Armendariz-Picon, Mukhanov & Steinhardt 2000). The dark energy fluid is typically characterized by the effective sound speed $c_{\rm s}$ and the transition regime between clustered and smooth dark energy is determined by the sound horizon (Hu & Scranton 2004). The clustering of dark energy acts as a source for gravitational potential wells; therefore, one finds the growth rate enhanced on scales above the sound horizon. In quintessence models $c_{\rm s}^2 = 1$; therefore, the sound horizon is equal to the particle horizon and the effect of this transition is not measurable. Nevertheless, in models with a smaller sound speed ($c_{\rm s}^2 \ll 1$) such as k-essence models, this transition may have detectable effects.[3]

Motivated by these arguments we introduce a method to measure the scale-dependence of the growth rate of structure using PV surveys. Observations from PVs are unique in this respect as they allow constraints on the growth rate on scales inaccessible to RSD measurements. This sensitivity is a result of the relation between velocity and density modes $v(k, z) \sim \delta(k, z)/k$ which one finds in Fourier space at linear order (Dodelson 2003). The extra factor of $1/k$ gives additional weight to velocities for larger scale modes relative to the density field. A further advantage arises because of the low redshift of PV surveys, namely that the Alcock–Paczynsi effect – transforming the true observables (angles and redshifts) to comoving distances – only generates a very weak model dependence.

A potential issue when modelling the velocity power spectrum is that it is known to depart from linear evolution at a larger scale than the density power spectrum (Scoccimarro 2004; Jennings, Baugh & Pascoli 2011). We pay particular attention to modelling the non-linear velocity field using two loop multipoint propagators (Bernardeau, Crocce & Scoccimarro 2008). Additionally, we suppress non-linear contributions by smoothing the velocity field using a gridding procedure. Using numerical N-body simulations, we validate that our constraints contain no significant bias from non-linear effects.

[1] Note in this analysis we will constrain the 'velocity power spectrum' which we define as a rescaling of the more conventional velocity divergence power spectrum (see Section 3).

[2] A scale-dependent growth rate can be indirectly tested using the influence the growth rate has on the halo bias (e.g. Parfrey, Hui & Sheth 2011).

[3] The presence of dark energy clustering requires some deviation from $w = -1$ in the low-redshift universe.

For our study, we use the recently compiled 6-degree Field Galaxy Survey velocity (6dFGSv) data set along with low-redshift SNe observations. The 6dFGSv data set represents a significant step forward in PV surveys; it is the largest PV sample constructed to date by a factor of ∼3, and it covers nearly the entire southern sky. We improve on the treatment of systematics and the theoretical modelling of the local velocity field, and explore a number of different methods to extract cosmological constraints. We note that the 6dFGSv data set will also allow constraints on the possible self-interaction of dark matter (Linder 2013), local non-Gaussianity (Ma, Taylor & Scott 2013), and the Hubble flow variance (Wiltshire et al. 2013).

The structure of this paper is as follows. In Section 2, we introduce the PV surveys we analyse; Section 3 describes the theory behind the analysis and introduces a number of improvements to the modelling and treatment of systematics effects. We validate our methods using numerical simulations in Section 4; the final cosmological constraints are presented in Section 5. We give our conclusion in Section 6.

2 DATA AND SIMULATED CATALOGUES

2.1 6dFGS peculiar velocity catalogue

The 6-degree Field Galaxy Survey (6dFGS) is a combined redshift and PV survey that covers the whole southern sky with the exception of the region within 10° of the Galactic plane. The survey was performed using the six-degree Field (6dF) multifibre instrument on the UK Schmidt Telescope from 2001 to 2006. Targets were selected from the *K*-band photometry of the 2MASS Extended Source Catalog (Jarrett et al. 2000). For full details see Jones et al. (2004, 2006, 2009). To create the velocity subsample from the full 6dF galaxy sample the following selection requirements were imposed: reliable redshifts (i.e. redshift quality $Q = 3$–5), redshifts less than $cz < 16120\,\mathrm{km\,s^{-1}}$ in the CMB frame, galaxies with early-type spectra, sufficiently high signal-to-noise ratio ($\mathrm{S/N} > 5\,A^{-1}$), and velocity dispersions greater than the instrumental resolution limit ($\sigma_0 \geq 112\,\mathrm{km\,s^{-1}}$). This sample represents the largest and most uniformly distributed PV survey to date (Fig. 1 top panel). The final number of galaxies with measured PVs is 8896 and the average fractional distance error is $\sigma_\mathrm{d} = 26$ per cent. The redshift distribution for 6dFGSv is given in Fig. 2. The PVs for 6dFGSv are derived using the FP relation (for details of the calibration of this relation see Magoulas et al. 2010, 2012). The complete 6dFGSv FP catalogue is presented in Campbell et al. (2014). Using the fitted FP relation, the final velocity catalogue is constructed in Springob et al. (in preparation). For each galaxy in the catalogue we determine a probability distribution for the quantity $\log_{10}(D_z/D_\mathrm{H})$; where D_z and D_H are, respectively, the 'observed' comoving distance inferred from the observed redshift and the true comoving distance.

2.2 Low-*z* SNe catalogue

To extend the velocity sample into the Northern hemisphere and cross-check the results for systematic errors, we construct a new homogeneous set of low-redshift Type Ia SNe. The sample contains SNe with redshifts $z < 0.07$ and the distribution on the sky is given in Fig. 1 (lower panel) and the redshift distribution is given in Fig. 2. The sample contains the following: 40 SNe from the Lick Observatory Supernova Search (LOSS) sample (Ganeshalingam et al. 2013) analysed using the SALT2 light-curve fitter; 128 SNe from Tonry et al. (2003); 135 SNe from the 'Constitution' set compiled by Hicken et al. (2009), where we choose to use the sample reduced using the multicolour light-curve shape method (MLCS) with their mean extinction law described by $R_v = 3.1$; 58 SNe in the Union sample from Kowalski et al. (2008);[4] 33 SNe from Kessler et al. (2009), where we use the sample derived using MLCS2k2 with $R_v = 2.18$; and finally 26 SNe are included from the Carnegie Supernova Project (Folatelli et al. 2010). Significant overlap exists between the samples, so for SNe with multiple distance modulus estimates we calculate the median value. This approach appears the most conservative given the lack of consensus between light-curve reduction methods and the correct value of R_v; nevertheless, we find there are no significant systematic offsets between the different reduction methods once we correct for zero-point offsets. The final catalogue consists of 303 SNe with an average fractional distance error, $\sigma_\mathrm{d} \sim 5$ per cent.

We update the redshifts in these samples with the host galaxy redshifts in the CMB frame given in the NASA Extragalactic Database, excluding SNe with unknown host galaxy redshifts; this is necessary as the quoted error in the redshift given for SNe data sets is similar to the typical effect that PVs have on the observed redshift. A number of these data sets include an error component $\sigma_\mathrm{v} \sim 300\,\mathrm{km\,s^{-1}}$ accounting for peculiar motion. Where applicable, we removed in quadrature this error component of $(5/\ln(10))\sigma_\mathrm{v}/cz$ from the distance modulus errors. This component is removed so that we can treat the samples uniformly, and in our analysis we treat the velocity dispersion as a free parameter. The estimated intrinsic scatter in absolute magnitude σ_SNe is included in the error budget in all the samples. We define $\delta m \equiv \mu_\mathrm{obs}(z) - \mu_\mathrm{Fid}(z)$, where μ_Fid is the distance modulus calculated in a homogeneous Friedmann-Robertson-Walker (FRW) universe at redshift, z, assuming the fiducial cosmology: $\Omega_\mathrm{b} = 0.0489$, $\Omega_\mathrm{m} = 0.3175$, $n_\mathrm{s} = 0.9624$, $w = -1.0$, $H_\mathrm{Fid} = 67\,\mathrm{km\,s^{-1}\,Mpc^{-1}}$ (motivated by Planck Collaboration XVI 2013).

For a consistent determination of the line-of-sight PV, S, and the quantity δm, the value of H_0 used to derive the prediction for the fiducial cosmology $\mu_\mathrm{Fid}(z)$ needs to be the same as the value assumed during the light-curve fitting procedure (where $\mu_\mathrm{obs}(z)$ is derived). The authors of different SNe samples have assumed different values of H_0 when deriving the distance moduli. Therefore, before calculating δm and the PV we correct this using $\Delta\mu_i = 5\ln(H_{0,i}/H_\mathrm{Fid})$, where $H_{0,i}$ is the assumed H_0 value in the ith sample and H_Fid is the expansion rate at which we choose to normalize the sample.[5] The assumed value of H_Fid here is simply used because it is a convenient normalization. As δm is a ratio of distances it is independent of the assumed value of H_0 (the values used to derive both distance moduli simply need to be equivalent).

For the rest of the paper, we set $H_0 = 100\,h\,\mathrm{km\,s^{-1}Mpc^{-1}}$. The line-of-sight PV is calculated as

$$S = \frac{\ln(10)}{5}\left(1 - \frac{(1+z)^2}{H(z)d_\mathrm{L}(z)}\right)^{-1}\delta m, \quad (1)$$

where $d_\mathrm{L}(z)$ is the luminosity distance and $H(z)$ the Hubble expansion rate calculated in the fiducial model at the observed redshift z (the derivation of this equation should be clear from equation 17).

[4] The new union2.1 data set adds no additional low-z SNe.

[5] In the order that the SNe samples have been introduced the assumed velocity dispersion values are $\sigma_\mathrm{v} = [300, 500, 400, 300, 300, 300]\,\mathrm{km\,s^{-1}}$ and the assumed values of the Hubble constant are $H_0 = [70, 65, 65, 70, 65, 72]\,\mathrm{km\,s^{-1}\,Mpc^{-1}}$.

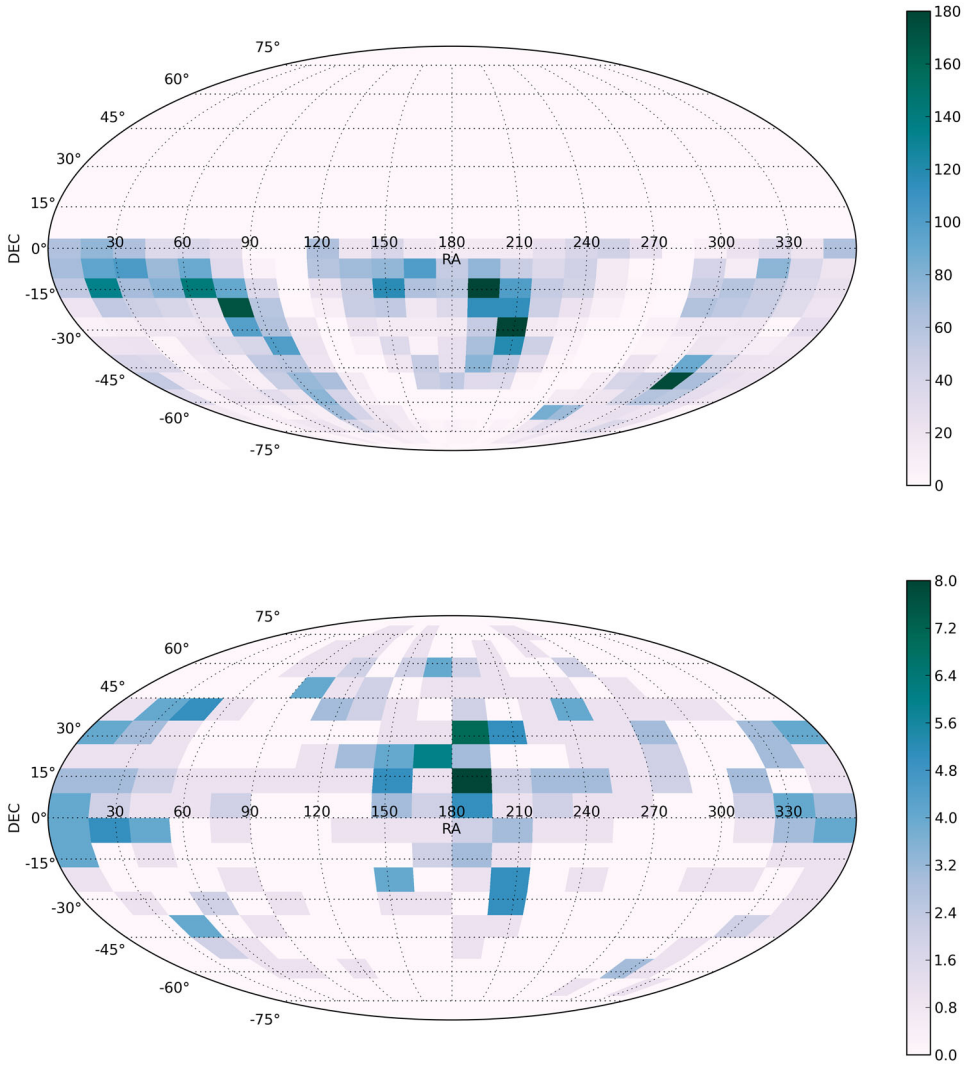

Figure 1. Mollweide projection of the 6dFGSv sample (upper) and the low-z SNe sample (lower) given in right ascension (RA) and declination (Dec.) coordinates. We grid the RA and Dec. coordinates on to a 25 × 25 grid for the upper plot and a 20 × 20 grid for the lower plot. The colour of each cell indicates the number of galaxies with measured PVs in that cell; as given by the colour bars on the right.

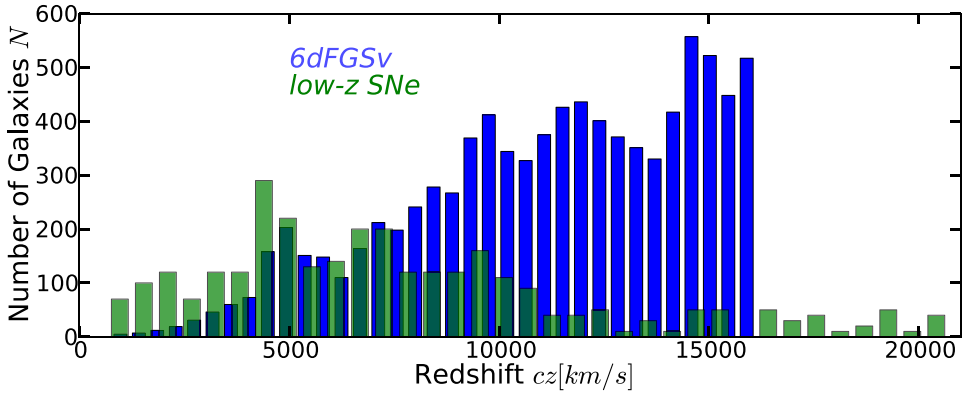

Figure 2. The redshift distribution for both the 6dFGSv and low-z SNe PV catalogues. Here we have scaled up the number count for the SNe sample in each redshift bin by a factor of 10 in order to allow the two distributions to be overplotted.

2.3 Mock catalogues

We construct two sets of mock catalogues (I) and (II) using the GiggleZ *N*-body simulation (Poole et al. 2014). The simulation was run inside a periodic box of 1 h^{-1}Gpc with 2160^3 particles of mass $7.5 \times 10^9 h^{-1} M_\odot$. The simulation used the GADGET2 code (Springel 2005), and haloes and subhaloes were identified using the SUBFIND algorithm (Springel et al. 2001). The simulation is run assuming a fiducial cosmology that is specified in Section 4. Using the GiggleZ simulations 10 non-overlapping realizations of PV surveys were constructed for both mock set (I) and (II), with the following properties.

(I) From each central 'observer' a random sample of ∼3500 dark matter haloes were selected within 100 h^{-1} Mpc from the full sample available in the simulation (i.e. full sky coverage). An uncertainty in the apparent magnitude of $\sigma_{\delta m} \sim 0.1$ was applied to each galaxy. This corresponds to a distance error of $\sigma_{\rm d} \sim 5$ per cent (viz. the approximate distance uncertainty for SNe).

(II) From each central observer ∼8000 dark matter haloes within 150 h^{-1} Mpc were selected from one hemisphere of the sky. An error in the apparent magnitude fluctuation was introduced by interpolating from the observed trend for the 6dFGSv galaxies of $\sigma_{\delta m}$ with redshift. Fitting a simple linear relationship to the 6dFGSv data we find $\sigma_{\delta m} = 0.51 + 2.985z$. The final range of introduced observational uncertainties is $\sigma_{\delta m} \sim [0.5, 0.75]$.

We subsample these haloes randomly from the chosen observer volumes. We limit the size of each hypothetical survey to reduce large-scale correlations between the individual realizations, although we expect that the catalogues may still contain residual correlations though being drawn from the same simulation. This situation is more severe for mock set (II). In general, the purpose of mock set (I) is to test the validity of our algorithms, various systematic effects and potential bias from non-linear effects, since the geometry (sky coverage) of the PV survey is not important, at first order, to answer these questions. Mock set (II) is used as an approximate realization of the 6dFGSv survey.

In the mock simulations, we apply a perturbation to the PVs that is similar to the scatter induced by observational error. The process proceeds as follows. We place an observer in the simulation box and extract from the simulation the line-of-sight velocity S and true comoving distance $D_{\rm H}$ of each surrounding galaxy. These quantities allow us to determine the observed redshift $z_{\rm obs}$, from $z_{\rm obs} = (1 + z_{\rm H})(1 + S/c) - 1$, and hence the observed redshift-space distance D_z. We now calculate the magnitude fluctuation $\delta m = 5 \log_{10}(D_z/D_{\rm H})$ and apply an observational Gaussian error, using the standard deviations specified above. We do not attempt to include additional effects such as survey selection functions, which are not required for the analysis described here.

3 THEORY AND NEW METHODOLOGY

Here we discuss a number of issues, including some improvements, in the framework for analysing PV surveys. We pay particular attention to the following:

(i) the covariance matrix of the data (Section 3.1),
(ii) the effects of non-Gaussian observational errors and the requirement, in order to have Gaussian observational errors, to use an underlying variable that is linearly related to the logarithmic distance ratio (Section 3.2),
(iii) the information we can extract from measurements of the local velocity field using 2-point statistics (Section 3.3),

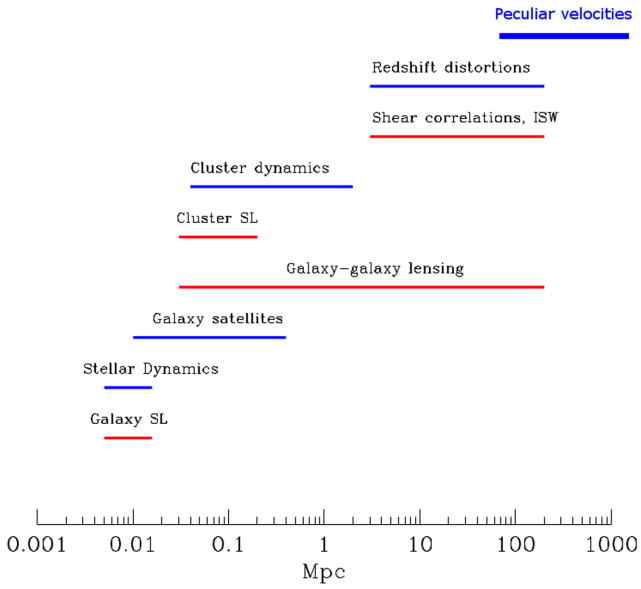

Figure 3. Scales probed by different methods to constrain gravity. The cosmological probes shown in red lines probe gravity by its effect on the propagation of light, i.e. weak and strong lensing (such measurements probe the sum of the spatial and temporal gravitational potential). Probes that use dynamical measurements are given as blue lines (these trace the temporal part of the gravitational potential). PVs probe the largest scales of any current probe. The figure is adapted from Lombriser et al. (2012).

(iv) modelling the velocity power spectrum, including non-linear effects in redshift space (Section 3.4),
(v) data compression using gridding methods (Section 3.5),
(vi) Marginalization of the unknown zero-point (Section 3.6) and
(vii) Combining different correlated data sets using hyperparameters (Section 3.7).

The goal of this analysis is quantifying and modelling the degree to which PVs fluctuate from one part of the universe relative to other spatially separated parts. The magnitude of this fluctuation in the PV field is generated by tidal gravitational fields which are in turn generated by the degree of departure from a homogeneous FRW metric and the relationship between density gradients and gravitational fields.

We introduce a method for extracting scale-dependent constraints on the normalized growth rate of structure $f\sigma_8(z, k)$. We emphasize the unique ability of PV measurements to probe the growth rate of structure on scales that are not currently accessible to RSD measurements, and the complementarity that exists between velocity surveys and RSD measurements in constraining modified gravity theories. Fig. 3 (adapted from Lombriser et al. 2012) shows the various length-scales probed by different methods to constrain gravity.

These methods can also be applied to larger upcoming PV surveys, such as the all-sky H I survey (WALLABY), the Taipan Fundamental Plane survey and the SDSS Fundamental Plane sample (Colless, Beutler & Blake 2013; Saulder et al. 2013) for which it will become even more crucial to extract unbiased results with accurate error estimates. Furthermore, the improvements considered here will be significant for other approaches for extracting information from velocity surveys, for example by using the cross-correlation between density and velocity fields.

3.1 Velocity covariance matrix

We start with the assumption that the velocity field is well described by a Gaussian random field, with zero mean. Therefore, considering a hypothetical survey of N galaxies each with a measured PV $S(\boldsymbol{x}, t) = \boldsymbol{v}(\boldsymbol{x}, t) \cdot \hat{r}$, one can write down the likelihood for observing this particular field configuration as

$$\mathcal{L} = \frac{1}{|2\pi C^{(v)}|^{1/2}} \exp\left(-\frac{1}{2}\sum_{m,n} S_m(\boldsymbol{x}, t) C^{(v)-1}_{mn} S_n(\boldsymbol{x}, t)\right), \tag{2}$$

where $\boldsymbol{v}(\boldsymbol{x}, t)$ is the total velocity of the object evaluated at the spatial position $\boldsymbol{x}$ and time t, and $\hat{r}$ is a unit vector in the direction of the galaxy. The desired (unknown) variable in this equation, which depends on the cosmological model, is the PV covariance matrix. By definition $C^{(v)}_{mn} \equiv \langle S_m(\boldsymbol{x}_m) S_n(\boldsymbol{x}_n)\rangle$. The validity of the assumptions described above will be discussed in later sections. The above approximation to the likelihood yields the probability of the velocity field configuration (the data d) given the covariance (as determined by the cosmological model m); this quantity is typically denoted $\mathcal{L} \equiv P(d|m)$. The quantity we are interested in extracting is the probability of the model given our observations of the velocity field, viz. $P(m|d)$. Bayes' theorem relates these two quantities as $P(m|d) = P(d|m)P(m)/P(d)$. $P(d)$ can be absorbed into a normalization factor and we assume a uniform prior (i.e. $P(m) = 1$), implying $P(m|d) \propto \mathcal{L}$.

The physical interpretation of the components of the covariance matrix is as follows: the diagonal elements can be viewed as representing cosmic variance (later we add a further diagonal contribution from observational uncertainties and non-linear contributions). As the model cosmology is changed, altering the degree of clustering in the low-redshift universe, the magnitude of cosmic variance changes. The covariance between individual PVs (i.e. the off-diagonal elements) results from those velocities being generated by the same underlying density field. Large wavelength Fourier density modes will have very similar phases for close pairs of galaxies; thus, a similar gravitational force will be exerted on these galaxies and therefore their PVs will be correlated.

Hitherto, the covariance matrix $C^{(v)}_{mn}$ has been calculated in terms of the matter power spectrum, $P(k)$. We suggest that a more natural approach is to express the covariance matrix in terms of the velocity divergence power spectrum. We define the velocity divergence as $\theta(\boldsymbol{x}, t) \equiv \nabla \cdot \boldsymbol{v}(\boldsymbol{x}, t)$, therefore $\boldsymbol{v}(\boldsymbol{k}) = -\mathrm{i}\theta(\boldsymbol{k})\frac{\boldsymbol{k}}{k^2}$, so the velocity covariance matrix is given by

$$\begin{aligned} &C^{(v)}_{mn}(\boldsymbol{x}_m, \boldsymbol{x}_n) \\ &= \int \frac{\mathrm{d}^3k}{(2\pi)^3} \mathrm{e}^{\mathrm{i}\boldsymbol{k}\cdot\boldsymbol{x}_m} \int \frac{\mathrm{d}^3k'}{(2\pi)^3} \mathrm{e}^{-\mathrm{i}\boldsymbol{k}'\cdot\boldsymbol{x}_n} \frac{(\hat{x}_m \cdot \boldsymbol{k})\,(\hat{x}_n \cdot \boldsymbol{k}')}{k'^2 k^2} \langle\theta(\boldsymbol{k})\,\theta^*(\boldsymbol{k}')\rangle \\ &= \frac{1}{2\pi^2} \int \mathrm{d}k \mathcal{P}_{\theta\theta}(k, a = 1) \int \frac{\mathrm{d}\Omega_k}{4\pi} \mathrm{e}^{\mathrm{i}\boldsymbol{k}\cdot(\boldsymbol{x}_m - \boldsymbol{x}_n)} \left(\hat{x}_m \cdot \hat{k}\right)\left(\hat{x}_n \cdot \hat{k}\right). \end{aligned} \tag{3}$$

The simplification results from $\langle\theta(\boldsymbol{k})\,\theta^*(\boldsymbol{k}')\rangle \equiv (2\pi)^3\delta^3(\boldsymbol{k} - \boldsymbol{k}')\mathcal{P}_{\theta\theta}(k)$, where $\mathcal{P}_{\theta\theta}(k)$ is the power spectrum of $\theta(\boldsymbol{x}, t)$, evaluated here at a redshift of zero. The advantage of this derivation is that one is not required to assume the linear continuity equation. The angular part of the integral in equation (3) defines the survey window function, explicitly

$$W(k, \alpha_{ij}, r_i, r_j) \equiv \int \frac{\mathrm{d}\Omega_k}{4\pi} \mathrm{e}^{\mathrm{i}\boldsymbol{k}\cdot(\boldsymbol{x}_i - \boldsymbol{x}_j)} \left(\hat{x}_i \cdot \hat{k}\right)\left(\hat{x}_j \cdot \hat{k}\right). \tag{4}$$

The analytic form for equation (4) is given in the appendix of Ma, Gordon & Feldman (2011) as

$$\begin{aligned} W(k, \alpha_{ij}, r_i, r_j) = {} & 1/3\left[j_0(kA_{ij}) - 2j_2(kA_{ij})\right]\hat{r}_i \cdot \hat{r}_j \\ & + \frac{1}{A^2_{ij}} j_2(kA_{ij}) r_i r_j \sin^2(\alpha_{ij}), \end{aligned} \tag{5}$$

where $\alpha_{ij} = \cos^{-1}(\hat{r}_i \cdot \hat{r}_j)$, $A_{ij} \equiv |\boldsymbol{r}_i - \boldsymbol{r}_j|$ and $\boldsymbol{r}_i$ is the position vector of the ith galaxy. The window function $W_{i,j}(k) \equiv W(k, \alpha_{ij}, r_i, r_j)$ is plotted in Fig. 4 for a number of galaxy pairs in the 6dFGSv catalogue. For convenience, we change the normalization of the

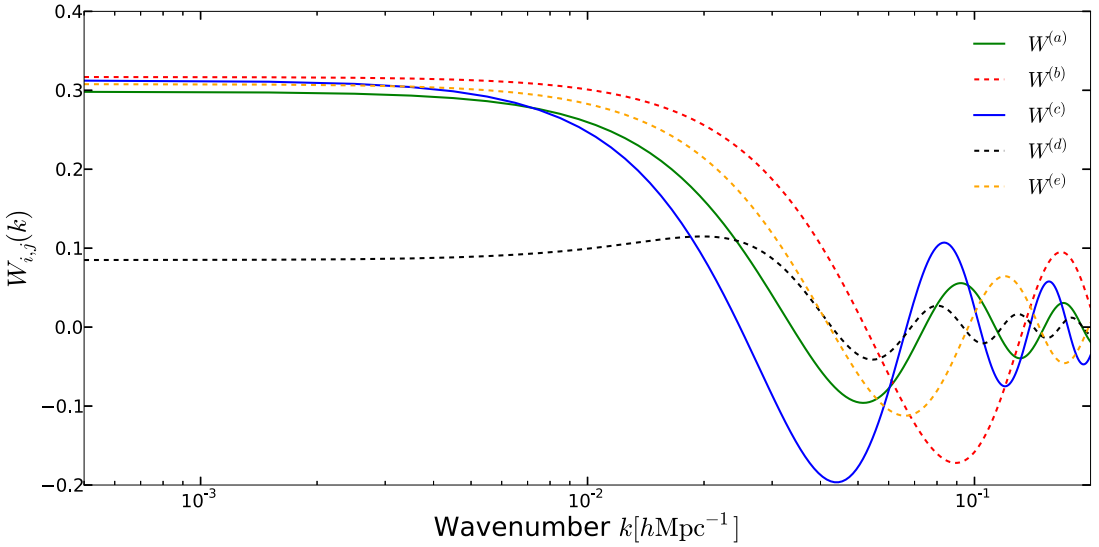

Figure 4. The window function for five pairs of galaxies in the 6dFGSv galaxy PV catalogue. Large-scale density fluctuations generate correlations between the PVs of pairs of galaxies, and the window function quantifies the wavelengths of density fluctuations that contribute to a given correlation. Specifically, the parameters input to the above window functions are as follows: for $W^{(a)}$ to $W^{(e)}$ we input $[r_i, r_j, \alpha]^{(a)} = [86.6, 133.7, 0.393]$, $[r_i, r_j, \alpha]^{(b)} = [76.8, 127.6, 1.313]$, $[r_i, r_j, \alpha]^{(c)} = [59.16, 142.5, 0.356]$,$[r_i, r_j, \alpha]^{(d)} = [51.9, 91.1, 0.315]$, and $[r_i, r_j, \alpha]^{(e)} = [99.49, 158.4, 0.463]$. The distances are all given in units of (h^{-1} Mpc) and angles in radians.

velocity divergence power spectrum and define the 'velocity power spectrum' as $\mathcal{P}_{vv}(k) \equiv \mathcal{P}_{\theta\theta}(k)/k^2$. Therefore, we have

$$C_{mn}^{(v)} = \int \frac{\mathrm{d}k}{2\pi^2} k^2 \mathcal{P}_{vv}(k, a=1) W(k, \alpha_{mn}, r_m, r_n). \quad (6)$$

3.2 The origin of non-Gaussian observational errors

Observations of the CMB have shown to a very high degree of accuracy that the initial density fluctuations in the universe are Gaussian in nature, which implies that the initial velocity fluctuations are also well described by a Gaussian random field. Linear evolution of the velocity field preserves this Gaussianity, as it acts as a simple linear rescaling. This simplifying property of large-scale density and velocity fields is often taken advantage of by approximations to the likelihood such as equation (2), which require that the PV field, S_i, be accurately described by a multivariate Gaussian distribution. Although this is true with regards to cosmic variance, a crucial issue is that *the observational uncertainty in PV surveys is often highly non-Gaussian in velocity units*. In this section, we describe the origin of this non-Gaussian error component, with particular reference to a FP survey; we note our conclusions are equally valid for Tully–Fisher data sets. Furthermore, we propose a solution to this problem and test its validity using numerical simulations in Section 4.

The FP relation is defined as $R_\mathrm{e} = \sigma_0^a \langle I_\mathrm{e} \rangle^b$, where R_e is the effective radius, σ_0 the velocity dispersion and $\langle I_\mathrm{e} \rangle$ is the mean surface brightness. In terms of logarithmic quantities it is defined as $r = as + bi + c$ ($r \equiv \log_{10}(R_\mathrm{e})$ and $i \equiv \log_{10}(\langle I_\mathrm{e} \rangle)$), where a and b describe the plane slope and c defines the zero-point. The FP relation therefore is a simple linear relation when the relevant variables are described in logarithmic units. Within this parameter space (or 'FP space') a 3D elliptical Gaussian distribution provides an excellent empirical fit to the observed scatter of the FP variables.[6] Changing the distance measure $\log_{10}(R_\mathrm{e})$ to a quantity not given in logarithmic units (i.e. simply R_e) one would find that the scatter of the new variables can no longer be described by a simple Gaussian distribution. This argument can be extended to the Tully–Fisher relation, as it has intrinsic scatter that appears to be modelled well by a Gaussian in absolute magnitude units.

As discussed in Springob et al. (in preparation) the fundamental quantity derived from the FP relation is the probability of a given ratio between the observed effective radius (observed size) R_z and the inferred physical radius (physical size) R_H of the specific galaxy viz. $P(\log_{10}(R_z/R_\mathrm{H}))$. In order to find the resulting probability distributions for PVs, $P(v_\mathrm{p})$, in standard units ($\mathrm{km\,s^{-1}}$) from the measured quantity $P(\log_{10}(R_z/R_\mathrm{H}))$ we need to calculate the Jacobian relating these two quantities. First, we can convert the logarithmic ratio of radii to a logarithmic ratio of comoving distances. Defining $x = \log_{10}(D_z/D_\mathrm{H})$, one has

$$\begin{aligned} P(x) &\equiv P\left(\log_{10}(D_z/D_\mathrm{H})\right) \\ &= J(D_\mathrm{H}, z_\mathrm{H}) P(\log_{10}(R_z/R_\mathrm{H})). \end{aligned} \quad (7)$$

The Jacobian term needed to transform the probability distribution from a size ratio to a distance ratio is approximated by (Springob et al., in preparation)

$$J(D_\mathrm{H}, z_\mathrm{H}) \approx \left(1 + \frac{99.939 D_\mathrm{H} + 0.01636 D_\mathrm{H}^2}{3 \times 10^5 (1+z_\mathrm{H})}\right), \quad (8)$$

where z_H is the Hubble redshift. Any dependence on the assumed cosmology here will be insignificant given the low redshifts of the observations. The probability distribution $P(x)$ is measured for each galaxy of the 6dFGSv survey using equation (7); importantly this distribution is very accurately described by a Gaussian distribution. Fig. 5 gives some examples for individual galaxies in the 6dFGSv sample.

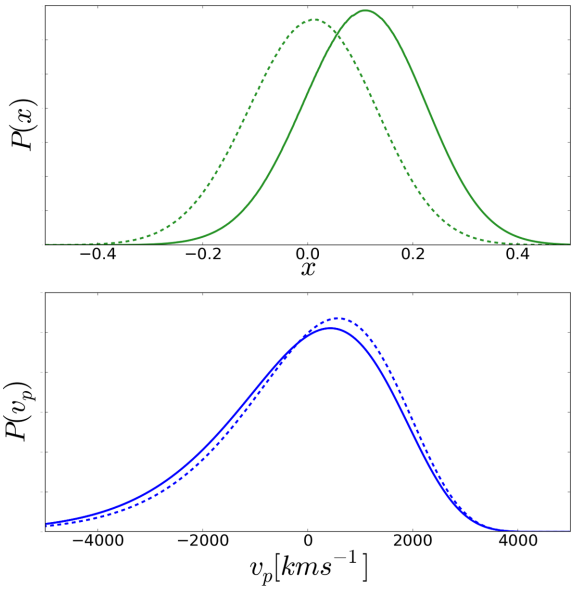

Figure 5. Probability distributions for $x = \log_{10}(D_z/D_\mathrm{H})$ and v_p for four 6dFGS velocity sample galaxies. We note that the distribution of x is well described by a Gaussian, whereas the distribution of v_p contains significant skewness.

We can now determine if the transformation from this distribution into the probability distribution for the PV (i.e. $P(x) \rightarrow P(v_\mathrm{p})$) preserves the Gaussian nature of the distribution or if it introduces non-Gaussianity. The transformation between these two probability distributions can be accurately approximated by

$$P(v) = P(x)\frac{\mathrm{d}x}{\mathrm{d}v} \approx P(x) \frac{(1+z_\mathrm{H})^2}{D_\mathrm{H} \ln(10) c (1+z)} \frac{\mathrm{d}D_\mathrm{H}}{\mathrm{d}z_\mathrm{H}}, \quad (9)$$

where $\mathrm{d}D_\mathrm{H}/\mathrm{d}z_\mathrm{H} = c/(99.939 + 0.016\,36 D_\mathrm{H})$.[7] Applying this non-linear transformation equation (9) to the $P(x)$ distributions given in the 6dFGSv sample we find the resulting velocity probability distributions, $P(v_\mathrm{p})$, become significantly skewed (as shown in Fig. 5) and hence are poorly described by a Gaussian distribution. In Section 4, we use numerical N-body simulations to quantify the impact of this non-Gaussianity on cosmological parameter fits, concluding that a measurable bias is introduced. To avoid this problem, one is required to adopt a variable for the analysis that is linearly related to the logarithm of the ratio of comoving distances.

[6] This scatter is generated by the PVs of the galaxies and the intrinsic scatter of the FP relation. Fig. 4 in Magoulas et al. (2012) shows the scatter of the FP parameters, where one can see the data is well described by a 3D elliptical Gaussian (see also Bernardi et al. 2003).

[7] This result can be derived from the approximation between comoving distance and redshift given in Hogg (in preparation), and is valid to <1 per cent within the range of redshift we are interested in.

3.2.1 Changing variables

The velocity variable we use is the apparent magnitude fluctuation, defined by $\delta m(z) = [m(z) - \bar{m}(z)]$, where both quantities are being evaluated at the *same* redshift (the observed redshift), see Hui & Greene (2006) and Davis et al. (2011). So the fluctuation is being evaluated with respect to the expected apparent magnitude in *redshift space*. The overbar here refers to the variable being evaluated within a homogeneous universe, i.e. in a universe with no density gradients and as a result no PVs. Recalling that the apparent magnitude is defined as

$$m = M + 5\log_{10}(d_{\rm L}(z)) + 25, \tag{10}$$

where M is the absolute magnitude and $d_{\rm L}(z)$ is the luminosity distance in parsecs, we find $\delta m(z) = 5x(z)$. We must now determine the covariance of magnitude fluctuations $C^{\rm m}_{ij} \equiv \langle \delta m_i(z_i)\delta m_j(z_j)\rangle$. The full treatment of this problem, which is effectively the derivation of the luminosity distance in a perturbed FRW universe, includes a number of additional physical effects besides peculiar motion that act to alter the luminosity distance, namely: gravitational lensing, the integrated Sachs–Wolfe effect, and gravitational redshift (Pyne & Birkinshaw 2004; Bonvin, Durrer & Gasparini 2006). For the relevant redshift range all these additional effects are currently insignificant. Here we focus on an intuitive derivation that captures all the relevant physics.

We first define the fractional perturbation in luminosity distance about a homogeneous universe as $\delta_{d_{\rm L}}(z) \equiv [d_{\rm L}(z) - \bar{d}_{\rm L}(z)]/\bar{d}_{\rm L}(z)$ and note from equation (10) that $\delta m = (5/\ln 10)\delta_{d_{\rm L}}$. Therefore, the problem is reduced to finding $C^{\rm L}_{ij} \equiv \langle \delta_{d_{\rm L}}(z_i)\delta_{d_{\rm L}}(z_j)\rangle$. The relationship between the observed flux F and the intrinsic luminosity L is given by

$$F(z) = \frac{L}{4\pi(1+z)^4}\frac{\delta\Omega_0}{\delta A_{\rm e}}, \tag{11}$$

where $\delta A_{\rm e}$ is the proper area of the galaxy (emitter) and $\delta\Omega_0$ is the observed solid angle. The angular diameter distance and the luminosity distance are defined as

$$d_{\rm A} = \sqrt{\delta A_e/\delta\Omega_0}, \quad d_{\rm L} = d_{\rm A}(1+z)^2, \tag{12}$$

both of which are valid in homogeneous and inhomogeneous universes[8] (Peebles 1993). In a homogeneous universe we have

$$\begin{aligned}\bar{d}_{\rm A}(\bar{z}) &= \chi_e/(1+\bar{z})\\ \chi_e \equiv \chi(\bar{z}) &= c\int_0^{\bar{z}} {\rm d}z'/H(z')\\ \bar{d}_{\rm L}(\bar{z}) &= \bar{d}_{\rm A}(\bar{z})(1+\bar{z})^2,\end{aligned} \tag{13}$$

where χ is the comoving distance and H is Hubble's constant. Introducing a PV component into this homogeneous system, i.e. perturbing the system, has two effects (at first order) as follows.

(i) The redshift of the object is perturbed (via the Doppler effect). For small velocities (i.e. $v < c$), as is applicable to local motions of galaxies, the relation between the redshift in the homogeneous universe $\bar{z}$ and the inhomogeneous universe z is given by

$$1 + z = (1+\bar{z})(1 + \boldsymbol{v}_{\rm e}\cdot\hat{n} - \boldsymbol{v}_0\cdot\hat{n}), \tag{14}$$

where $\boldsymbol{v}_{\rm e}$ is the emitting galaxy's velocity, $\boldsymbol{v}_0$ is the observer's velocity relative to the CMB, and $\hat{n}$ is a unit vector in the direction of the emitter from the absorber.

(ii) The angular diameter distance is changed as a result of relativistic beaming. This occurs as the angle of the galaxy is shifted by $\delta\Omega_0 \rightarrow \delta\Omega_0(1 - 2\boldsymbol{v}_0\cdot\hat{n})$. The result is

$$d_{\rm A}(z) = \bar{d}_{\rm A}(\bar{z})(1 + v_0\cdot\hat{n}). \tag{15}$$

Using equations (12), (14) and (15) the luminosity distance in the perturbed universe is given by

$$d_{\rm L}(z) = \bar{d}_{\rm L}(\bar{z})(1 + 2v_{\rm e}\cdot\hat{n} - v_0\cdot\hat{n}). \tag{16}$$

Taylor expanding $\bar{d}_{\rm L}(z)$ about $\bar{z}$ gives (Hui & Greene 2006)

$$\delta_{d_{\rm L}}(z) = \frac{\delta d_{\rm L}}{d_{\rm L}} = \hat{r}\cdot\left(\boldsymbol{v}_{\rm e} - \frac{(1+z)^2}{H(z)d_{\rm L}}[\boldsymbol{v}_e - \boldsymbol{v}_0]\right), \tag{17}$$

where we work in units with $c = 1$. This relation is accurate to first order in perturbation theory, ignoring other contributions. Our Galaxy's motion is very accurately known from observations of the CMB therefore we can transform the observed PV to the CMB rest frame and correct for the effect of v_0.[9] Given $\delta m = (5/\ln 10)\,\delta_{d_{\rm L}}$ and using equation (6) one finds

$$\begin{aligned}C^{\rm m}_{ij} = &\left(\frac{5}{\ln 10}\right)^2\left(1 - \frac{(1+z_i)^2}{H(z_i)d_{\rm L}(z_i)}\right)\left(1 - \frac{(1+z_j)^2}{H(z_j)d_{\rm L}(z_j)}\right)\\ &\times\int\frac{{\rm d}k}{2\pi^2}k^2\mathcal{P}_{vv}(k, a=1)W(k,\alpha_{ij},r_i,r_j).\end{aligned} \tag{18}$$

In Section 3.5, we update the formula for the covariance matrix to account for a smoothing of the velocity field we implement; the updated formula is given in equation (30).

3.2.2 Including the intrinsic error

To complete the covariance matrix of magnitude fluctuations we must add the observational part of the errors, uncorrelated between objects. This has two different components: the error in the measured apparent magnitude fluctuation $\sigma_{\rm obs}$ and a stochastic noise contribution $\sigma_{\rm v}$, which is physically related to non-linear contributions to the velocity (Silberman et al. 2001). The total magnitude scatter per object is given by

$$\sigma_i^2 = \sigma_{\rm obs}^2 + \left(\frac{5}{\ln 10}\right)^2\left(1 - \frac{(1+z_i)^2}{H(z_i)d_{\rm L}(z_i)}\right)^2\sigma_{\rm v}^2. \tag{19}$$

The updated posterior distribution is therefore given by

$$P(\Sigma|\boldsymbol{\delta m}) = |2\pi\Sigma|^{-1/2}\exp\left(-\frac{1}{2}\boldsymbol{\delta m}^{\rm T}\Sigma^{-1}\boldsymbol{\delta m}\right), \tag{20}$$

where

$$\Sigma_{ij} \equiv C^{\rm m}_{ij} + \sigma_i^2\delta_{ij}, \tag{21}$$

where $\boldsymbol{\delta m}$ is a vector of the observed apparent magnitude fluctuation. For the SNe sample $\sigma_{\rm obs}$ represents both the light-curve fitting error and the intrinsic dispersion, as derived by the original

[8] For completeness we note that the term inhomogeneous universe is used somewhat liberally in this section, the term should be taken to refer to a weakly perturbed Friedmann–Lemaître–Robertson–Walker geometry. In the context of general inhomogeneous universes the nature of the luminosity distance relation is unknown in most cases, and other physical contributions may become significant.

[9] We assume that the correlation between 'our' motion and nearby galaxies is insignificant (i.e. $\langle v_{\rm e}v_0\rangle = 0$). This is justified given we are working in the CMB frame. Any residual correlations when working in this reference frame are introduced by the effects of relativistic beaming which is a function of our local motion.

SNe analysis. We do not need to vary $\sigma_{\rm obs}$ as a free parameter because its effect is degenerate with the contribution from the velocity dispersion, which we allow to vary.

3.3 Methods to extract information from the local velocity field

The aim of this section is to outline the parametrizations of the velocity covariance matrix (equation 18) we consider, and hence the type of cosmological models we constrain.

3.3.1 Traditional parametrizations

We first discuss two different methods already present in the literature. Both compare data to model by calculating a model-dependent covariance matrix, but they differ in the power spectrum model used to generate that covariance matrix. In the first method, power spectra are generated for a range of cosmological models (as described below), while in the second method the power spectra are generated in a single fiducial cosmological model, and then perturbed in a series of Fourier bins. The first method is more easily compared directly to physical models, while the second allows detection of generic scale-dependent effects.

Within the standard cosmological model the velocity power spectrum $\mathcal{P}_{vv}(k)$ can be calculated as a function of the cosmological parameters (σ_8, $\Omega_{\rm m}$, $\Omega_{\rm b}$, $n_{\rm s}$, w, H_0). The parameters not previously described are defined as follows: $\Omega_{\rm b}$ is the baryon density divided by the critical density; $n_{\rm s}$ describes the slope of the primordial power spectrum; w is the dark energy equation of state; and H_0 is the current expansion rate. Current velocity data sets do not contain enough statistical power to constrain all these parameters, therefore we focus on the two most relevant parameters: σ_8, which describes the overall normalization and $\Omega_{\rm m}$, which controls the scale-dependence of power. Therefore, we fix ($\Omega_{\rm b} = 0.0489$, $n_{\rm s} = 0.9624$, $w = -1.0$ and $H_0 = 67\,{\rm km\,s^{-1}\,Mpc^{-1}}$) to the best-fitting *Planck* values (see e.g. Planck Collaboration XVI 2013). Now we can parametrize the velocity power spectrum as $\mathcal{P}_{vv}(k) = \mathcal{P}_{vv}(k, \Omega_{\rm m}, \sigma_8)$, and from equations (18) and (19) we can predict the covariance matrix as a function of these cosmological parameters, $\Sigma = \Sigma(\Omega_{\rm m}, \sigma_8)$, such that

$$P(\Omega_{\rm m}, \sigma_8|\boldsymbol{\delta m}) = |2\pi\Sigma(\Omega_{\rm m}, \sigma_8)|^{-1/2} \times \exp\left(-\frac{1}{2}\boldsymbol{\delta m}^{\rm T}\Sigma^{-1}(\Omega_{\rm m}, \sigma_8)\boldsymbol{\delta m}\right). \quad (22)$$

Note that the quantity $|2\pi\Sigma(\Omega_{\rm m}, \sigma_8)|$ depends on the cosmological parameters, as a result we do not expect the posterior distributions to be exactly Gaussian. Similar parametrizations were explored by Zaroubi et al. (2001), Zehavi & Dekel (2000) and Jaffe & Kaiser (1995).

The second method involves specifying a fiducial velocity power spectrum $\mathcal{P}^{\rm Fid}_{vv}(k)$ which we choose using the current best-fitting *Planck* constraints, explicitly ($\Omega_{\rm m} = 0.3175$, $\sigma_8 = 0.8344$, $\Omega_{\rm b} = 0.0489$, $n_{\rm s} = 0.9624$, $w = -1.0$, $\rm H_0 = 67\,km\,s^{-1}\,Mpc^{-1}$). The power spectrum is now separated into bins in Fourier space and a free parameter A_i is introduced and allowed to scale the 'power' within the given k range of a bin. One can hence constrain the amplitude of the velocity power spectrum in k-dependent bins. This parametrization is similar in nature to that explored in Macaulay et al. (2012) and Silberman et al. (2001), although the specifics of the implementation are somewhat different. This approach is more model independent than the first parametrization because it allows more freedom in the shape of the velocity power spectrum. Considering a case with N different bins, we define the centre of the ith bin as $k_i^{\rm cen}$ and the bin width as $\Delta_i \equiv \left(k_i^{\rm max} - k_i^{\rm min}\right)$. We define

$$\Pi(k, \Delta_i, k_i^{\rm cen}) \equiv \mathcal{H}(k - (k_i^{\rm cen} - \Delta_i/2)) - \mathcal{H} \times \left(k - \left(k_i^{\rm cen} + \Delta_i/2\right)\right), \quad (23)$$

where $\mathcal{H}(x)$ is a Heaviside step function, so $\Pi(k, k_i^{\rm cen}, \Delta_i)$ is equal to one if k is in the ith bin and zero otherwise. Including the free parameters A_i which scale the amplitude of the velocity power spectrum within each bin, the *scaled* velocity power spectrum is given by[10]

$$\mathcal{P}^{\rm Scaled}_{vv}(k) \equiv A_1\mathcal{P}^{\rm Fid}_{vv}(k)\Pi(k, \Delta_1, k_1^{\rm cen}) + A_2\mathcal{P}^{\rm Fid}_{vv}(k)\Pi(k, \Delta_2, k_2^{\rm cen}) \ldots + A_N\mathcal{P}^{\rm Fid}_{vv}(k)\Pi(k, \Delta_N, k_N^{\rm cen}). \quad (24)$$

The free parameters A_i do not have any k-dependence, and as a result one finds

$$\int \frac{{\rm d}k}{2\pi^2}k^2\mathcal{P}^{\rm Scaled}_{vv}(k)W(k, \alpha_{12}, r_1, r_2) = \sum_{i=1}^{N} A_i \int_{k_i^{\rm cen}-\Delta_i/2}^{k_i^{\rm cen}+\Delta_i/2} \frac{{\rm d}k}{2\pi^2}k^2\mathcal{P}^{\rm Fid}_{vv}(k)W(k, \alpha_{12}, r_1, r_2)$$

so the magnitude covariance matrix for the *scaled* velocity power spectrum is given by

$$C^m_{ij}(A_1, A_2, \ldots, A_N) = \left(\frac{5}{\ln 10}\right)^2\left(1 - \frac{(1+z_i)^2}{H(z_i)d_{\rm L}(z_i)}\right) \times \left(1 - \frac{(1+z_j)^2}{H(z_j)d_{\rm L}(z_j)}\right)\sum_{i=1}^{N} A_i \int_{k_i^{\rm cen}-\Delta_i/2}^{k_i^{\rm cen}+\Delta_i/2} \times \frac{{\rm d}k}{2\pi^2}k^2\mathcal{P}^{\rm Fid}_{vv}(k)W(k, \alpha_{i,j}, r_i, r_j).$$

From equations (20) and (21) we then have

$$P(A_1, A_2, \ldots, A_N|\boldsymbol{\delta m}) = |2\pi\Sigma(A_1, A_2, \ldots, A_N)|^{-1/2} \times \exp\left(-\frac{1}{2}\boldsymbol{\delta m}^{\rm T}\Sigma^{-1}(A_1, A_2, \ldots, A_N)\boldsymbol{\delta m}\right). \quad (25)$$

The best-fitting values A_i can be used to check the consistency with the fiducial model ($A_i = 1$) or to obtain the effective measured power $\mathcal{P}_i$ in each bin:

$$\mathcal{P}_i = A_i \int_{k_i^{\rm cen}-\Delta_i/2}^{k_i^{\rm cen}+\Delta_i/2} {\rm d}k\frac{\mathcal{P}_{vv}(k)}{\Delta_i}. \quad (26)$$

The $\mathcal{P}_i$ values can now be compared with the predictions of the velocity power spectrum from different cosmological models.

3.3.2 Scale-dependent growth rate

We can also relate the measured A_i values to the growth rate of structure at each scale, as follows.

Here we will assume linear perturbation theory to be valid for both the density and the velocity fields; the justification for this assumption will be given in Section 3.5. In this regime, the linear continuity equation is valid, i.e. $\theta(k) = -fH\delta(k)$. These assumptions are required to place constraints on the growth rate, but *not* required for the previous parametrizations. A shift in $f(z)\sigma_8(z)$ from the

[10] Note we have by definition

$$\mathcal{P}^{\rm Fid}_{vv}(k) = \mathcal{P}^{\rm Fid}_{vv}(k)\Pi(k, \Delta_1, k_1^{\rm cen}) + \mathcal{P}^{\rm Fid}_{vv}(k)\Pi(k, \Delta_2, k_2^{\rm cen}) \cdots + \mathcal{P}^{\rm Fid}_{vv}(k)\Pi(k, \Delta_N, k_N^{\rm cen}).$$

fiducial value to a new value, viz. $f\sigma_8(z)^{\rm Fid.} \rightarrow f\sigma_8(z)$, has an effect on the velocity divergence power spectrum that can be calculated as $\mathcal{P}_{\theta\theta}(k) \rightarrow A_1 \mathcal{P}_{\theta\theta}(k)$, where $A_1 = (f\sigma_8(z)/f\sigma_8(z)^{\rm Fid})^2$. One can then write down a 'scaled' velocity divergence power spectrum as

$$\begin{aligned}\mathcal{P}^{\rm Scaled}_{\theta\theta}(k) \equiv & \left(f\sigma_8(z,k_1^{\rm cen})/f\sigma_8(z)^{\rm Fid}\right)^2 \mathcal{P}^{\rm Fid}_{\theta\theta}(k)\Pi(k,\Delta_1,k_1^{\rm cen}) \\ & + \left(f\sigma_8(z,k_2^{\rm cen})/f\sigma_8(z)^{\rm Fid}\right)^2 \mathcal{P}^{\rm Fid}_{\theta\theta}(k)\Pi(k,\Delta_2,k_1^{\rm cen}) \\ & \ldots + (f\sigma_8(z,k_N^{\rm cen})/f\sigma_8(z)^{\rm Fid})^2 \mathcal{P}^{\rm Fid}_{\theta\theta}(k)\Pi(k,\Delta_N,k_N^{\rm cen}),\end{aligned} \tag{27}$$

where again $\mathcal{P}^{\rm Scaled}_{vv}(k) \equiv \mathcal{P}^{\rm Scaled}_{\theta\theta}(k)/k^2$, and there are N different bins that span the entire k range. The growth rate is considered to be constant over the wavenumber range of a given bin. The above relation equation (27) results from the approximation $\mathcal{P}_{\theta\theta}(k,z) \propto (\sigma_8 f(k,z))^2$.

The velocity power spectrum is calculated (at $z = 0$) by assuming the standard ΛCDM expansion history and that the growth of perturbations is governed by GR. We note that modifying the expansion history and/or deviations from GR at higher redshifts will affect the current growth rate. Therefore, in order to consistently examine the possibility of a scale-dependence of the growth rate of structure (i.e. moving beyond a consistency test) such effects would need to be taken into account. Such an approach is beyond the scope of this paper and left for future work; here we simply consider if the observed growth rate as a function of scale is consistent with that expected within the framework of the standard model.

3.4 Modelling of the velocity power spectrum

In this section, we will outline the model we use for the velocity power spectrum in terms of the cosmological parameters.

We calculate the real-space velocity power spectrum using the code VELMPTBREEZE (an extension of MPTBREEZE in Crocce, Scoccimarro & Bernardeau 2012), which computes the velocity power spectrum using two loop multipoint propagators (Bernardeau et al. 2008) in a similar way to renormalized perturbation theory (RPT; Crocce & Scoccimarro 2006). VELMPTBREEZE uses an effective description of multipoint propagators introduced in Crocce et al. (2012) which significantly reduces computation time relative to other RPT implementations. The results from VELMPTBREEZE were extensively tested against N-body simulations (Crocce & Scoccimarro, in preparation).

3.5 Reducing non-linear systematics and computation time

The velocity field is directly driven by the tidal gravitational field $\nabla\Phi$, where Φ is the gravitational potential, which causes it to depart from the linear regime at larger scales than the density field (Scoccimarro 2004). While the off-diagonal elements of the covariance matrix equation (30) are dominated by large-scale modes, as a result of the survey geometry,[11] this is not the case for the diagonal (cosmic variance) elements where the small-scale power contributes to the intrinsic scatter. Hence, non-linear effects are important to consider and minimize.

In order to suppress non-linear contributions and hence reduce potential systematic biases we adopt a simple smoothing (gridding) procedure. Gridding the velocity field significantly reduces the computation time by reducing the size of the covariance matrix; this will be essential for next-generation data sets given the computational demands of the likelihood calculation (which requires a matrix inversion for each likelihood evaluation).

The binning method we implement was developed and tested in Abate et al. (2008). The grid geometry used is a cube of length L, where the average apparent magnitude fluctuation δm and error $\sigma_{\delta m}$ are evaluated at the centre of the ith grid cell $\boldsymbol{x}_i$:

$$\begin{aligned}\delta m_i(\boldsymbol{x}_i) &= \frac{1}{N_i}\sum_j \delta m^{\rm gal}_j(\boldsymbol{x}_j)\Theta_{ij}, \\ \sigma_{\delta m,i} &= \frac{1}{N_i^{3/2}}\sum_j \sigma^{\rm gal}_{\delta m,j}\Theta_{ij},\end{aligned} \tag{28}$$

where N_i is the number of galaxies located within the ith cell, $\delta m^{\rm gal}$ is the inferred fluctuation in apparent magnitude for a specific galaxy and $\sigma^{\rm gal}_j$ is the error component as defined in equation (19). The optimal choice for the gridding length-scale is evaluated using numerical simulations and is discussed in Section 4. Both the observational error from the distance indicators and the error introduced by the non-linear velocity dispersion $\sigma_{\rm v}$ are being averaged. The sum over j is taken over the entire sample, where Θ_{ij} equals one when the galaxy is within the grid cell and zero otherwise. The process of smoothing the velocity field effectively damps the velocity power spectrum, this acts to suppress non-linear contributions. The function describing this damping is given by the Fourier transform of the kernel Θ_{ij}, introduced in equation (28). Letting $\Gamma(k) \equiv \mathcal{F}[\Theta_{ij}]$ from above we have

$$\Gamma(k) = \left\langle \mathrm{sinc}\left(k_x\frac{L}{2}\right)\mathrm{sinc}\left(k_y\frac{L}{2}\right)\mathrm{sinc}\left(k_z\frac{L}{2}\right)\right\rangle_{k\in k}, \tag{29}$$

where $\langle F(\boldsymbol{k})\rangle_{k\in k}$ is the expectation value of $F(\boldsymbol{k})$ in the phase space $\boldsymbol{k} \in k$, i.e. $\langle F(\boldsymbol{k})\rangle_{k\in k} = 1/4\pi \int \mathrm{d}\Omega F(\boldsymbol{k})$. Examples of $\Gamma(k)^2$, for a range of different smoothing scales, are given in Fig. 6. This allows one to calculate the velocity power spectrum between separate grid points; therefore, once the velocity field has been smoothed we alter the theoretical prediction of the velocity power spectrum

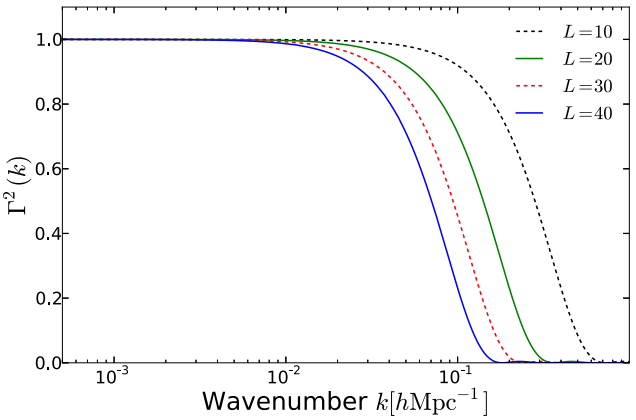

Figure 6. Examples of the smoothing kernel $\Gamma(k) \equiv \mathcal{F}[\Theta_{ij}]$ for different values of the smoothing length L, given in units of h^{-1} Mpc. We plot the square of the kernel as this is the term that modulates the velocity power spectrum, i.e. the term occurring in equation (30).

[11] This can be seen when plotting the window function $W(k) \equiv (\sum_{j=1}^{N}\sum_{i=1}^{N} W(k,\alpha_{ij},r_i,r_j))/N^2$ of the survey (where $W(k,\alpha_{ij},r_i,r_j)$ is defined in equation 5) and N is the number of galaxies in the survey. This window function only influences off-diagonal elements of the covariance matrix. One finds that the amplitude of $W(k)$ significantly reduces as small scales are approached, therefore less weight is attached to the power spectrum on small scales.

by $\mathcal{P}_{vv}(k) \rightarrow \mathcal{P}_{vv}^{\rm Grid}(k) = \mathcal{P}_{vv}(k)\Gamma^2(k)$. Now the covariance of δm between grid centres, $\tilde{C}_{ij}$, is given by

$$\tilde{C}_{ij} = \left(\frac{5}{\ln 10}\right)^2 \left(1 - \frac{(1+z_i)^2}{H(z_i)d_{\rm L}(z_i)}\right)\left(1 - \frac{(1+z_j)^2}{H(z_j)d_{\rm L}(z_j)}\right) \times \int \frac{{\rm d}k}{2\pi^2} k^2 \mathcal{P}_{vv}(k, a=1) W(k, \alpha_{ij}, r_i, r_j)\Gamma^2(k). \quad (30)$$

Using numerical N-body simulations Abate et al. (2008) explore the dependence of the recovered best-fitting parameters (σ_8 and $\Omega_{\rm m}$) on the smoothing length. Specifically, they find that (relative to the statistical error) a smoothing scale greater than $10\,h^{-1}$ Mpc results in an unbiased estimation of the cosmological parameters of interest.

In order to derive equation (30) one must pre-suppose that the PVs inside each cell are well described as a continuous field. However, the velocities inside a grid cell represent discrete samples from the PV field; therefore, as the number density inside each cell becomes small this approximation becomes worse. In Abate et al. (2008) a solution to this 'sampling problem' was proposed and tested using N-body simulations. To mitigate the effects of this approximation one interpolates between the case of a discrete sample and that of the continuous field limit. The weight attached to each is determined using the number of galaxies within each cell N_i. The diagonal elements of the covariance matrix are now updated as

$$\tilde{C}_{ii} \rightarrow \tilde{C}_{ii} + (\tilde{C}_{ii} - C_{ii}^{\rm m})/N_i, \quad (31)$$

where $C_{ii}^{\rm m}$ is defined in equation (18). For this correction, the continuous field approximation is assumed for the off-diagonal elements.[12]

3.6 Effect of the unknown zero-point

The zero-point in a PV analysis is a reference magnitude, or size in the case of FP surveys, for which the velocity is known to be zero. From this reference point, one is able to infer the velocities of objects; without such a reference point only the relative velocities could be determined. An incorrectly calibrated zero-point introduces a monopole component to measured PVs. To give an example, for SNe the zero-point is determined by the absolute magnitude M and the Hubble parameter H_0.

When deriving PV measurements the zero-point is typically fixed at its maximum likelihood (ML) value found during the calibration phase of the analysis; this allows the velocities of all the objects in the sample to be determined. However, this zero-point may contain error. In this section, we introduce a method to analytically propagate the uncertainty in the zero-point into the final cosmological result.

We first consider the case of analysing a single velocity survey. We define a as an offset in the magnitude fluctuation, such that $\delta m \rightarrow \delta m + a$. This indirectly represents a perturbation to the velocity zero-point. Given we have some prior knowledge of the distribution of this variable we give it a Gaussian prior, i.e.

$$P(y|\sigma_y) = \frac{1}{(2\pi)^{1/2}\sigma_y} \exp\left[-y^2/2\sigma_y^2\right]. \quad (32)$$

We define $\boldsymbol{x}$ as an N dimensional vector where each element is set to one (i.e. $(\boldsymbol{x})_i = 1$, for $i = 1, \ldots, N$). Here N is the dimension of $\boldsymbol{\delta m}$. The parameter a alters the theoretical prediction for the mean velocity, $\langle \boldsymbol{\delta m}^p \rangle = 0$, to $\langle \boldsymbol{\delta m}^p \rangle = y\boldsymbol{x}$. Now we can analytically marginalize over the unknown zero-point (Bridle et al. 2002)

$$P(\Sigma|\boldsymbol{\delta m}) = \int {\rm d}y\, P(\Sigma|\boldsymbol{\delta m}, y) P(y|\sigma_y) = |2\pi\Sigma|^{-1/2}(1 + \boldsymbol{x}^T\Sigma^{-1}\boldsymbol{x}\sigma_y^2)^{-1/2} \exp\left[\frac{1}{2}\boldsymbol{\delta m}^T\Sigma_M^{-1}\boldsymbol{\delta m}\right], \quad (33)$$

where

$$\Sigma_M^{-1} \equiv \Sigma^{-1} - \frac{\Sigma^{-1}\boldsymbol{x}\boldsymbol{x}^{\rm T}\Sigma^{-1}}{\boldsymbol{x}^{\rm T}\Sigma^{-1}\boldsymbol{x} + \sigma_y^{-2}}. \quad (34)$$

We may wish to combine a number of different PV surveys with potentially different zero-point offsets. In this case, it is necessary to consider how one can marginalize over the independent zero-points simultaneously. We consider the example of two different PV surveys but note that this approach can be readily generalized to a larger number of surveys (Bridle et al. 2002).

First we decompose the data vector into apparent magnitude fluctuations from the first and second surveys,

$$\boldsymbol{\delta m} = \begin{pmatrix} \boldsymbol{\delta m}^{(1)} \\ \boldsymbol{\delta m}^{(2)} \end{pmatrix}_N, \quad (35)$$

where the first survey has n_1 data points and the second has n_2, therefore the combined vector has length $N = n_1 + n_2$. The data from the two surveys need to be smoothed on to two different grids, this is a simple modification to the binning algorithm:

$$\boldsymbol{\delta m} = \begin{pmatrix} \frac{1}{N_{1,i}} \sum_{j \le n_1} \delta m_j^{\rm gal}(\boldsymbol{x}_j)\Theta_{ij} \\ \frac{1}{N_{2,i}} \sum_{n_1 < j \le n_2} \delta m_j^{\rm gal}(\boldsymbol{x}_j)\Theta_{ij} \end{pmatrix}, \quad (36)$$

where $N_{1,i}$ and $N_{2,i}$ are the number of galaxies inside the ith cell from the first and second survey, respectively.

We now introduce two free parameters (y, b) which will allow the zero-point to vary for each survey, again both parameters are given Gaussian priors (i.e. are distributed according to equation 32). To account for a changing zero-point we alter the theoretical prediction for the mean value of the apparent magnitude fluctuations $\langle \boldsymbol{\delta m}^p \rangle$. This quantity is normally set to zero as PVs are assumed to be distributed according to a multivariate Gaussian with a mean of zero, now we have $\langle \boldsymbol{\delta m}^p \rangle = y\boldsymbol{x}^{(1)} + b\boldsymbol{x}^{(2)}$, where $x_i^{(1)} = 1$ if $i \le n_1$ and $x_i^{(1)} = 0$ otherwise and $x_i^{(2)} = 1$ if $i \ge n_1$ and $x_i^{(2)} = 0$ otherwise. The updated likelihood is then

$$P(\Sigma|\boldsymbol{\delta m}, y, b) = |2\pi\Sigma|^{-1/2} \times \exp\left(-\frac{1}{2}\left(\boldsymbol{\delta m} + \langle \boldsymbol{\delta m}^p \rangle\right)^{\rm T}\Sigma^{-1}\left(\boldsymbol{\delta m} + \langle \boldsymbol{\delta m}^p \rangle\right)\right).$$

We desire a posterior distribution independent of the zero-point corrections therefore we analytically marginalize over these parameters

$$P(\Sigma|\boldsymbol{\delta m}) = \int {\rm d}y \int {\rm d}b\; P(\Sigma|\boldsymbol{\delta m}, y, b) P(y|\sigma_y) P(b|\sigma_b) = |2\pi\Sigma|^{-1/2}(1 + \boldsymbol{x}^{(1)^T}\Sigma^{-1}\boldsymbol{x}^{(1)}\sigma_y^2)^{-1/2} \times (1 + \boldsymbol{x}^{(2)^T}\Sigma^{-1}\boldsymbol{x}^{(2)}\sigma_b^2)^{-1/2} \exp\left[\frac{1}{2}\boldsymbol{\delta m}^T\Sigma_M^{-1}\boldsymbol{\delta m}\right], \quad (37)$$

[12] This approach is valid given the off-diagonal elements of the covariance matrix are significantly damped at small scales, and hence the smoothing of the velocity field has only a small effect on these elements.

where

$$\Sigma_M^{-1} \equiv \Sigma^{-1} - \frac{\Sigma^{-1}\boldsymbol{x}^{(1)}\boldsymbol{x}^{(1)^{\rm T}}\Sigma^{-1}}{\boldsymbol{x}^{(1)^{\rm T}}\Sigma^{-1}\boldsymbol{x}^{(1)}} - \frac{\Sigma^{-1}\boldsymbol{x}^{(2)}\boldsymbol{x}^{(2)^{\rm T}}\Sigma^{-1} + \sigma_y^{-2}}{\boldsymbol{x}^{(2)^{\rm T}}\Sigma^{-1}\boldsymbol{x}^{(2)} + \sigma_b^{-2}}. \quad (38)$$

Here we need to consider the variation to the determinant as the covariance matrix is being varied at each likelihood evaluation. For all zero-points here we choose a Gaussian prior with a standard deviation of $\sigma_y = \sigma_b = 0.2$. We find the choice of width of the prior has an insignificant effect on the final results.

3.7 Combining multiple (correlated) velocity surveys

Given the limited number count and sky coverage of objects in velocity surveys it is common for different surveys to be combined in a joint analysis. In this situation, individual data sets may contain unrecognized systematic errors, requiring them to be reweighted in the likelihood analysis.

The first method we consider to do this is a recent upgrade to the hyperparameter analysis. The original hyperparameter method was developed to remove the inherent subjectivity associated with selecting which data sets to combine in an analysis and which to exclude (see Lahav et al. 2000; Hobson, Bridle & Lahav 2002). This process is achieved by including all the available data sets but allowing free hyperparameters to vary the relative 'weight' attached to each data set, the hyperparameters are then determined in a Bayesian way. Consider two hypothetical surveys with chi-squared of $\chi^2_{\rm A}$ and $\chi^2_{\rm B}$. The combined constraints are typically found by minimizing the quantity

$$\chi^2_{\rm com} = \chi^2_{\rm A} + \chi^2_{\rm B}. \quad (39)$$

This gives both data sets equal weight. Introducing the hyperparameters one has

$$\chi^2_{\rm com} = \alpha\chi^2_{\rm A} + \beta\chi^2_{\rm B}. \quad (40)$$

The hyperparameters can be interpreted as scaling the errors for each data set, i.e. $\sigma^i \rightarrow \sigma_i\alpha^{-1/2}$, or equivalently the covariance matrix of each data set $C_i \rightarrow \alpha^{-1}C_i$. The final values of the hyperparameters, more accurately their probability distributions $P(\alpha)$ and $P(\beta)$, give an objective way to determine if there are systematic effects present in the data (e.g. a value $\alpha > 1$ can be interpreted as reducing the errors or correspondingly increasing the relative weight of the data set).

The problem with the traditional hyperparameter analysis for PV surveys is that it assumes that the individual data sets are *not correlated* (this assumption is required to write down equation equations 39 and 40). If the surveys cover overlapping volumes or are influenced by the same large-scale modes this is not the case. Recently the hyperparameter formalism has been extended to a hyperparameter matrix method which includes the cross-correlations between surveys (Ma & Berndsen 2013). Here the hyperparameters scale both the covariance between objects in a given data set and the covariance between the data sets:

$$C^{D_iD_j} \rightarrow \left(\alpha_i\alpha_j\right)^{-1/2} C^{D_iD_j}, \quad (41)$$

where D_i represents the ith data set, so $C^{D_iD_j}$ gives the covariance between the ith and jth data sets. For simplicity, here we outline the case of two different data sets. In this case, there are two hyperparameters (α_1, α_2) which we treat as free parameters. The hyperparameter matrix is defined as

$$H = \begin{pmatrix} \alpha_1^{-1} & (\alpha_1\alpha_2)^{-1/2} \\ (\alpha_1\alpha_2)^{-1/2} & \alpha_2^{-1} \end{pmatrix}. \quad (42)$$

The final likelihood function is

$$P(\boldsymbol{\delta m}|\boldsymbol{\theta}, \boldsymbol{\alpha}) = \left[\prod_{i=1}^{2}\left(\frac{\alpha_i}{2\pi}\right)^{n_i/2}\right]\frac{1}{\sqrt{|C|}}\exp\left(-\frac{1}{2}\delta m^T\left(\hat{H}\odot C^{-1}\right)\delta m\right).$$

Here $\odot$ is an 'element-wise' product (or Hadamard product) defined as $(\hat{H}\odot C^{-1})_{ij} = \hat{H}_{ij} \times (C^{-1})_{ij}$ and $\boldsymbol{\theta}$ represents the parameters of interest. $\hat{H}$ is the Hadamard inverse of the 'hyperparameter' matrix (i.e. $\hat{H}_{ij} = P_{ij}^{-1}$), and n_1 and n_2 are the number of data points in the first and second surveys, respectively.

As described in Section 3.2.2 a free parameter $\sigma_{\rm v}$ is typically introduced to account for non-linear random motion. One issue with the likelihood function defined above is that $\sigma_{\rm v}$ and the hyperparameters are quite degenerate. Therefore, for our hyperparameter analysis, we fix $\sigma_{\rm v}$ at the values found when analysing the surveys independently.

4 TESTING WITH SIMULATIONS

We require simulations of PV catalogues for several aspects of this analysis. First, to determine if non-linear effects from the growth rate of structure or RSDs cause systematic errors. Secondly, to determine the approximate survey geometry and distance errors for which the non-Gaussian observational scatter of PVs becomes important. Finally, to determine the effect (on the final constraints) of marginalizing over the zero-point uncertainty. Note the construction of the mock catalogues used in this section is outlined in Section 2.

All the cosmological parameters not allowed to vary freely here are set to those input into the simulation (i.e. $\Omega_\Lambda = 0.727$, $\Omega_{\rm m} = 0.273$, $\Omega_k = 0$, $H_0 = 100\,h\,{\rm km\,s^{-1}\,Mpc^{-1}}$, $\sigma_8 = 0.812$, $n_{\rm s} = 0.960$). For the velocity power spectrum fits we use a smoothing scale (defined in Section 3.5) of $10\,h^{-1}$ Mpc, while for the analysis of $\Omega_{\rm m}$ and σ_8 we adopt a length of $20\,h^{-1}$ Mpc. We use a larger grid size for the analysis of $\Omega_{\rm m}$ and σ_8 because the evaluation of the likelihood (i.e. equation 22) is more computationally demanding relative to the evaluation of the likelihood given in equation (25), the larger grid size reduces the computational requirements.[13] We first shift the haloes within the simulation to their redshift-space position, using $\boldsymbol{x}^s = \boldsymbol{x}^r + \boldsymbol{v}(\boldsymbol{x}, t)\cdot\hat{r}/H_0$. Now we transform the PVs within the simulation to apparent magnitude fluctuations, δm.

At small scales the predictions from RPT become less accurate and are known to break down (experience exponential damping relative to the expectations from N-body simulations) at $k \sim 0.15\,h\,{\rm Mpc^{-1}}$ for the velocity power spectrum evaluated assuming the fiducial cosmology of the simulation at a redshift of zero. We therefore truncate the velocity power spectrum fits at this scale. We note that this scale varies for different cosmological parameters, therefore for the $(\Omega_{\rm m}, \sigma_8)$ fits we test a range of values, $k_{\rm max}$, for truncating the integral when calculating the covariance matrix, to decide the optimal choice for the data.

Now using eight different observers from mock set (I) we test the ability of each parametrization to recover the input cosmology, under the conditions outlined above. Recall for mock set (I) the input distance error is $\sigma_{\rm d} \sim 5$ per cent, the approximate distance error for SNe. The derived constraints on $(\Omega_{\rm m}, \sigma_8)$ for various values of $k_{\rm max}$ are given in Fig. 7; the black square symbols here give the

[13] This is the case because for each $\Omega_{\rm m}$ and σ_8 posterior evaluation we are required to recalculate the entire covariance matrix (equation 30). This is not the case for the other parametrizations considered here.

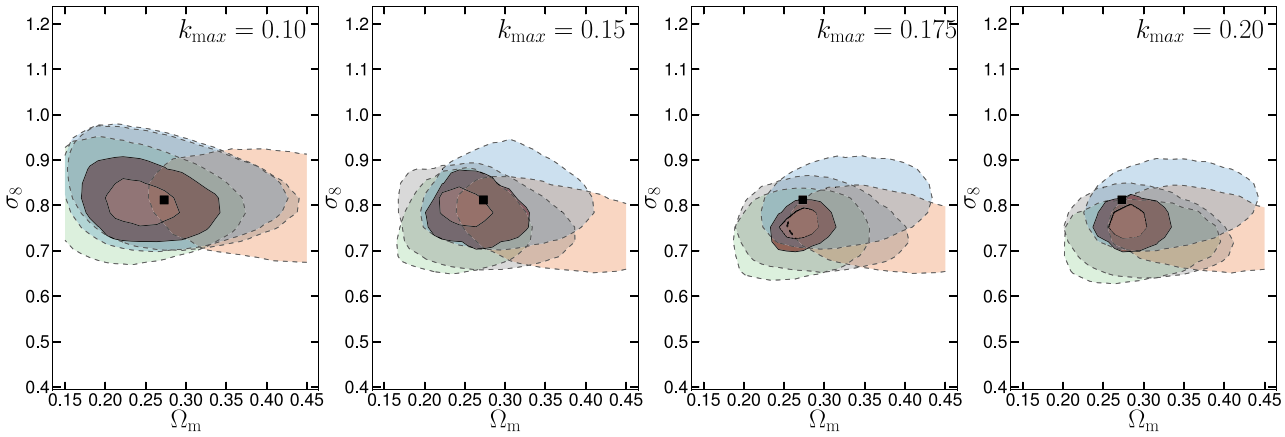

Figure 7. 68 per cent confidence regions for the matter density, Ω_m, and the rms clustering in $8\,h^{-1}$ Mpc spheres, σ_8, using mock set (I), including RSD and using the δm variable. The transparent contours (dashed outline) give the constraints from some example single-survey realizations. The opaque contours (solid outline) give the combined constraints from eight realizations. For the combined constraints, we give 68 and 95 per cent confidence regions. A smoothing length of $20\,h^{-1}$ Mpc is used for all constraints. For each plot, we vary the length-scale, k_{max} at which we truncate the integral for the calculation of the covariance matrix, that is the integral given in equation (30) (i.e. the smallest scales included in the analysis). Varying this scale allows us to test the validity of the constraints as we move into the non-linear regime. From left to right the wavenumbers at which we cut off the integration are $k_{max} = [0.1, 0.15, 0.175, 0.20]\,h$ Mpc^{-1}. The black square symbols give the cosmology input into the simulation.

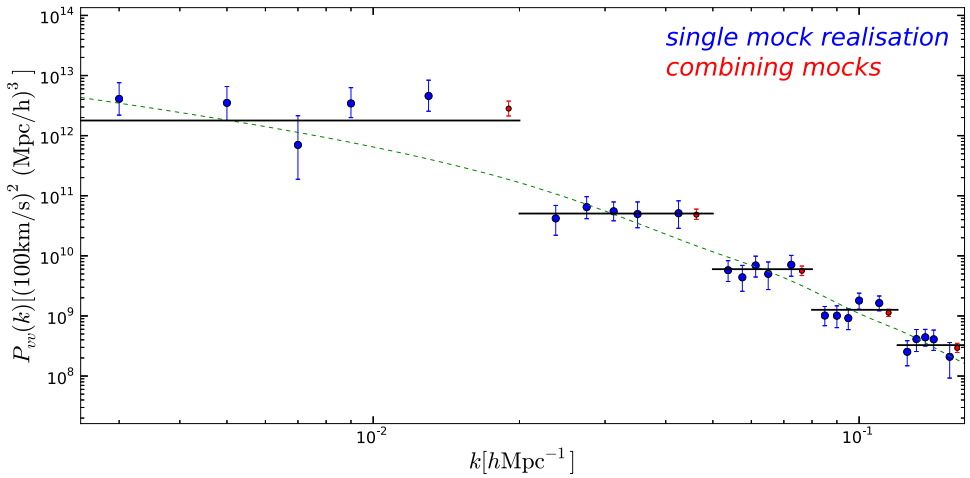

Figure 8. 68 per cent confidence intervals for the amplitude parameters A_i describing the mean 'power' within each bin using mock set (I). The thick blue (horizontal) lines give the mean power in each bin for the fiducial cosmology calculated using equation (26). Here we include RSDs, use δm and a smoothing length of $10\,h^{-1}$ Mpc. The blue points are the constraints found for individual mock realizations, while the red points show the constraints found by combining the results from eight different mocks. Consistency with the assumed fiducial cosmology occurs when the given confidence levels overlap with the mean power; the specific position of the point along the bin length is arbitrary. The green dashed line shows the velocity power spectrum calculated assuming the fiducial cosmology. Section 5.3 gives the wavenumber bin intervals used here, with the exception that $k_{min} = 0.0065\,h$ Mpc$^{-1} = 2\pi/L_{box}$.

input cosmology of the simulation. The velocity power spectrum measurements are given in Fig. 8 and the constraints for a scale-dependent growth rate, $f\sigma_8(z = 0, k)$, are given in Fig. 9. The thick blue lines in Fig. 8 give the predictions for the average power within the defined bin ranges for the fiducial cosmology, this is calculated using equation (26) with $A_i = 1$. In addition to giving the results for a single mock realization we also average the results found for eight different mock realizations in order to provide a more accurate systematic test. Again some care needs to be taken when interpreting the combined constraints given that on the largest scales the mock realizations are *significantly correlated*. This is most pronounced for the largest scale bin in Figs 8 and 9, for which we interpret the consistently 'high' measurement power as being produced by correlations. Also note the mock simulations considered here have *significantly* greater statistical power than current PV surveys, so we are performing a sensitive systematic check. We find that at the investigated error levels we are able to accurately recover the input cosmology of the simulation for all parametrizations considered. We conclude therefore that the bias from non-linear structure is currently insignificant, the linear relation between the PV and δm is valid and non-linear RSD effects do not bias our final constraints.

Following Fig. 8, we conservatively fix $k_{max} = 0.15\,h$ Mpc^{-1} for the (Ω_m, σ_8) fits, given that on smaller scales we observe a slight trend away from the fiducial cosmology (yet still consistent at the 2σ level). For the power spectrum fits, we note a small amount of correlation exists between the different wavenumber bins. We give a typical example of the correlation coefficients between the bins in Fig. 10, determined using the Markov chain Monte Carlo (MCMC).

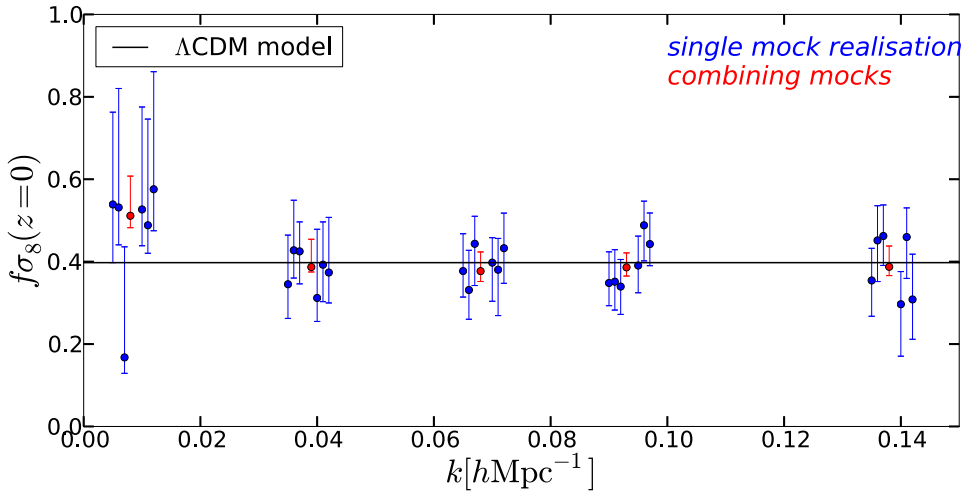

Figure 9. 68 per cent confidence intervals for the normalized *scale-dependent* growth rate $f(z=0,k)\sigma_8(z=0)$ in five different bins in Fourier space. The thick black line gives the prediction of the input cosmology. For each k-bin, we plot the results from six different realizations from mock set (I). We include RSDs in the mocks, use the variable δm, and choose a smoothing length of $10\,h^{-1}$ Mpc. The specific k-values within a given bin for the measurements are arbitrary. The bin intervals used here are given in Section 5.3, with the one correction that $k_{\rm min} = 0.0065\,h^{-1}$ Mpc, corresponding to the size of the simulation.

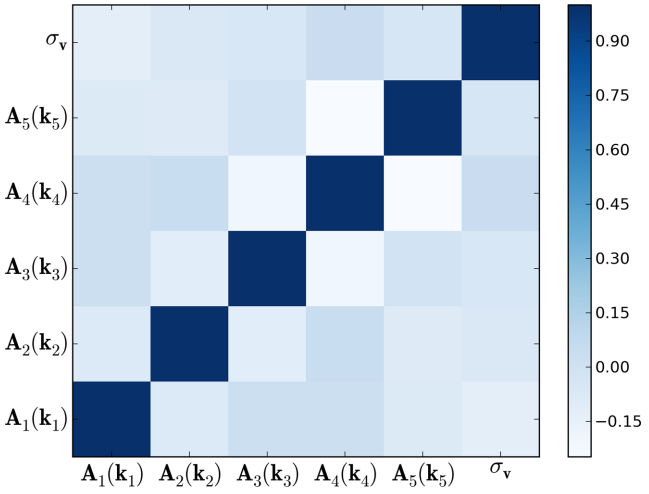

Figure 10. Correlation coefficients r between the amplitude parameters A_i, and the non-linear velocity dispersion $\sigma_{\rm v}$. The results here were calculated using an MCMC chain (of length $\sim 10^6$) produced when analysing a single realization from mock set (I). We expect very similar correlations to exist between the growth rate measurements and note that the correlations between the different bins are quite weak.

When testing the effect of non-Gaussian observational error for PVs, both the sky coverage of the survey and the distance error are relevant, therefore we consider both mock set (I) and (II). We find that for mock set (I) using the velocity not magnitude as the variable in the analysis results in no significant bias. This continues to be true even when we limit the survey to one hemisphere. This can be understood because the degree of departure from Gaussianity of the probability distribution of PVs, $P(v)$, is dependent on the magnitude of the distance error. With relatively small distance errors, $P(v_{\rm p})$ is described well by a Gaussian distribution.

In the case of a distance and sky distribution corresponding to 6dFGSv, that is, $\sigma_{\rm d} \sim 30$ per cent and only considering one hemisphere (i.e. mock set II) we find a *significant* bias is introduced when using PVs.[14] We use eight realizations from mock set (II), generate realistic observational errors and perform the likelihood analysis twice using either PV or δm as the variable. For the likelihood analysis using PV one is required to input a single velocity value, which gives us some freedom in how we choose to compress the distribution $P(v_{\rm p})$ into a single value. Here we consider the mean, ML and median. For a detailed investigation into the effect of these choices, in the context of bulk flow measurements, see Scrimgeour et al. (in preparation). In all prior PV analysis, when the full probability distribution of the distance measure (e.g. the absolute magnitude, M, in the case of the Tully–Fisher relation) was not available the PV was calculated directly from this variable. The Jacobian term is ignored in this case, we label this method the 'direct approach'. To give an example for the FP relation using this direct method one would determine the ML value of $x \equiv \log_{10}(D_z/D_{\rm H})$ then using this value calculate the corresponding PV, again ignoring the Jacobian term given in equation (9).

We give the constraints for the amplitude of the velocity power spectrum and the cosmological parameters σ_8 and $\Omega_{\rm m}$, found when using the magnitude fluctuation δm, in Fig. 11. For the fits of σ_8 and $\Omega_{\rm m}$ we also use the mean of $P(v_{\rm p})$ and the direct method; while for the velocity power spectrum fits we use the median of $P(v_{\rm p})$ (viz. $v_i = \mathrm{Median}[P(v_i)]$). Here we have combined the constraints from different mock realizations. Note for the separate fits using δm and the PV we have used the same mock realizations. We interpret the slight offset from the fiducial model (still within 1σ) of the constraints found using δm as simply a result of cosmic variance and covariance between mock realizations.

We conclude that for the constraints on σ_8 and $\Omega_{\rm m}$ using the mean, median and ML of $P(v_{\rm p})$ and the direct method in the likelihood analysis all introduce a significant bias (i.e. $>2\sigma$) in the final cosmological parameter values when considering a radial and angular halo distribution similar to 6dFGSv (and averaging over eight realizations). We find a similar, yet less significant, bias for the velocity power spectrum, given the derived constraints are now

[14] This also applies for future analyses; a number of FP and Tully–Fisher surveys are forthcoming and will have similar properties.

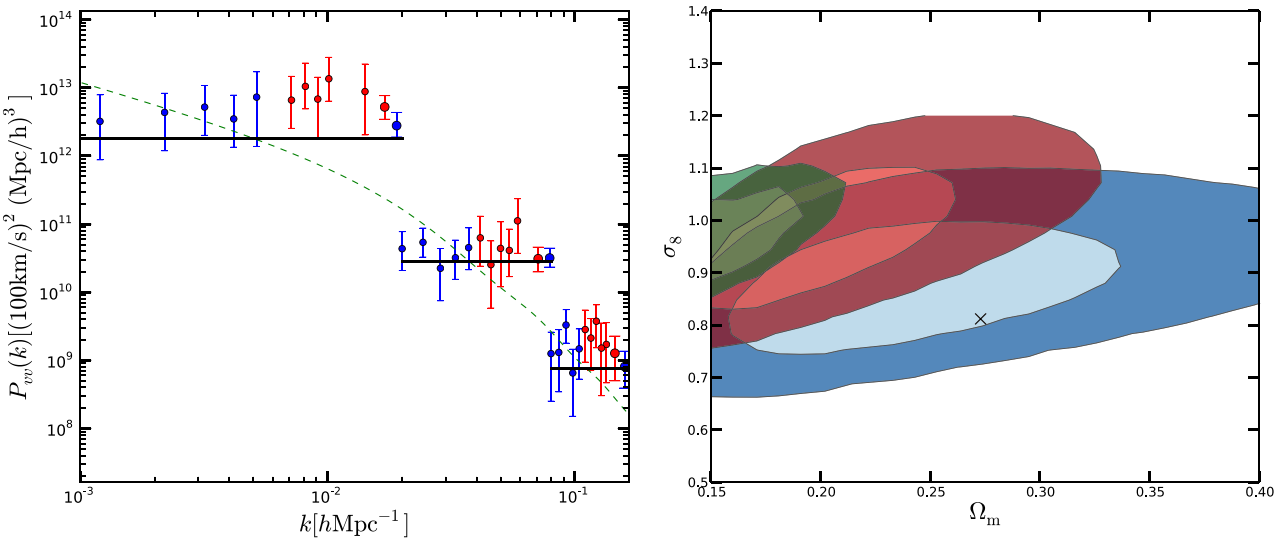

Figure 11. Left: 68 per cent confidence intervals for the velocity power spectrum amplitude in three Fourier bins. We consider five separate realizations taken from mock set (II). The small blue points show the individual constraints found using the variable δm, while the small red points show the constraints found using the median of the velocity distributions (viz. $v_i = \mathrm{Median}[P(v_i)]$) (this gives very similar results to the direct method). The larger blue and red points show the results from combining the five realizations. The circle symbols (left-hand panel) give the median value of the probability distributions. Right: constraints on the parameters Ω_m and σ_8 found from combining the results from eight different realizations with mock set (II). The contours give 68 and 95 per cent confidence levels. The blue contour shows the result of using the variable δm. The red and green contours show the result of using the PV as the main variable, where the red contour gives the result from directly calculating the PV from the observable quantity ignoring the Jacobian term, and the green contour gives the constraints from using the mean value of $P(v)$.

consistent at the 2σ level. As shown in the left-hand panel of Fig. 11, the result is *more power* relative to the fiducial cosmology on the largest scales, which is consistent with a low bias in Ω_m. The non-Gaussian distributions imprint a bias in the mean radial velocity and therefore influence power on the largest scale. Once a full sky survey is considered this effect is less severe as the bias tends to average out.

We test the sensitivity of the final constraints to the process of marginalizing over the zero-point. We find that the final results are reasonably insensitive to this procedure. As expected, the error in measurements on the largest scales is increased, which slightly weakens the constraints in the largest scale bin for the growth rate and velocity power spectrum measurements, and equivalently weakens the constraints on the matter density Ω_m.

5 PARAMETER FITS TO VELOCITY DATA SETS

In this section, we present the results from the analysis of the 6dFGSv and low-z SNe PV surveys. Analysing the fluctuations in the measured PVs and their correlations (as a function of their spatial separation) we are able to derive constraints on the following: the cosmological parameters Ω_m and σ_8 (Section 5.2); the amplitude of the velocity power spectrum, $\mathcal{P}_{vv}(k) \equiv P_{\theta\theta}(k)/k^2$ in a series of (five) $\Delta k \sim 0.03\,h\,\mathrm{Mpc}^{-1}$ bins (Section 5.3); the scale-dependent normalized growth rate of structure, $f\sigma_8(z=0,k)$, in a series of (five) $\Delta k \sim 0.03h\,\mathrm{Mpc}^{-1}$ bins (Section 5.4); and the scale-independent growth rate of structure, $f\sigma_8(z=0)$ (Section 5.4). All the constraints given are at a redshift $z \sim 0$. We emphasize that, because we have not included any information from the local density field, as inferred by the local distribution of galaxies, the results presented here do *not* rely on any assumptions about galaxy bias. Additionally, here we are working solely within the standard ΛCDM model.

For Sections 5.2–5.4 we give the results derived when analysing the individual surveys separately. Comparing the results from different PV surveys allows one to check for systematic effects. When combining the PV surveys we consider two different approaches, both introduce extra degrees of freedom that allow the relative 'weight' of each sample to vary in the likelihood calculation. First, we introduce a free parameter σ_v to each survey, this term accounts for non-linear velocity dispersion. Secondly, we allow the relative weight of each survey to be varied by the use of a matrix hyperparameter method (introduced in Section 3.7). In this case, we fix the σ_v values of both surveys to the ML values found when analysing the surveys separately. The purpose of the hyperparameter analysis is to check the statistical robustness of our constraints. In the case that the hyperparameter analysis is statistically consistent with the standard method of combining the surveys we quote the results from the standard method as our final measurement. The two PV samples we use for this analysis have significant overlap, therefore we expect the individual results to be highly correlated, given they share the same cosmic variance. This limits the benefits from combining the samples. In addition, complications arise when data points from each survey are placed on the same grid point, as occurs when the velocity surveys are separately smoothed on to grids.[15]

For all likelihood calculations in the following sections we marginalize over the unknown zero-point[16] (i.e. a monopole contribution to the velocity field). The result of this process is that our constraints are not sensitive to the uncertainties present in the determination of the zero-point in PV surveys and the assumptions required to determine the zero-point.

[15] We treat these data points as if they were perfectly correlated in the full covariance matrix.

[16] We allow each survey to have different zero-point offsets for the marginalization.

5.1 MCMC sampling strategy

To sample the posterior distributions, we use a python implementation of the affine-invariant ensemble sampler for MCMC MCMC-HAMMER (Foreman-Mackey et al. 2013). This technique was introduced by Goodman & Weare (2010). We use the MCMC-HAMMER algorithm because, relative to the standard Metropolis–Hastings (M–H) algorithm the integrated autocorrelation time is lower and less 'tuning' is required; specifically, only two parameters are required to tune the performance of the Markov chain, as opposed to $N[N+1]/2$ parameters in M–H, where N is the dimension of the parameter space. Additionally, the MCMC-HAMMER algorithm is trivially parallelized using `MPI` and the *affine invariance* (invariance under linear transformations) property of this algorithm means it is independent of covariances between parameters[17] (Foreman-Mackey et al. 2013).

We discard the first 20 per cent of each chain as 'burn in' given that the sampling may be non-Markovian, while the convergence of each chain is assessed using the integrated autocorrelation time. From the samples, we generate an estimate of the posterior ML and median; given the posterior distributions of the parameters tend to be non-Gaussian, the 68 per cent confidence intervals we quote are found by calculating the 34 per cent limits about the estimated median. In the case where we cannot quote a robust lower bound, when the probability distribution peaks near zero, we quote 95 per cent upper limits.

5.2 Matter density and clustering amplitude

The base set of parameters we allow to vary in this analysis is [$\Omega_{\rm m}$, σ_8, $\sigma_{\rm v}$]. In the case, where we combine PV surveys we consider two extensions to this base set. First, we include a free parameter modelling the non-linear velocity dispersion $\sigma_{\rm v}$ for each survey and therefore consider the set of parameters [$\Omega_{\rm m}$, σ_8, $\sigma_{v,1}$, $\sigma_{v,2}$]. Secondly, we fix the values for the velocity dispersion and introduce hyperparameters, this gives the set [$\Omega_{\rm m}$, σ_8, $\alpha_{\rm 6dF}$, $\alpha_{\rm SNe}$].

For each likelihood evaluation of the cosmological parameters we must compute the corresponding velocity power spectrum. While the calculation of the velocity power spectrum in VELMPTBREEZE is significantly faster than previous RPT calculations, it remains too slow to embed directly in MCMC calculations. Therefore, the approach we take here is to pre-compute a grid of velocity power spectra then use a bilinear interpolation between the grid points to estimate the power spectra.

Using VELMPTBREEZE we evaluate a grid of velocity power spectra; we use the range $\Omega_{\rm m} = [0.050, 0.500]$ and $\sigma_8 = [0.432, 1.20]$, which act as our priors. We use step sizes of $\Delta\Omega_{\rm m} = 0.01$ and $\Delta\sigma_8 = 0.032$. We do not investigate the region of parameter space where $\Omega_{\rm m} < 0.05$ as here the theoretical modelling of the velocity power spectrum becomes uncertain as it becomes highly non-linear on very large scales. The prior placed on all $\sigma_{\rm v}$ parameters is $\sigma_{\rm v} = [0, 1000]$ km s^{-1} and $\alpha_i = [0, 10]$. For each value of $\Omega_{\rm m}$, the matter transfer function needs to be supplied, to do this we use the CAMB software package (Lewis, Challinor & Lasenby 2000). The numerical integration over the velocity power spectrum requires us to specify a k-range. Here we integrate over the range $k = [0.0005, 0.15]\,h\,{\rm Mpc}^{-1}$. We note that integrating to larger scales (i.e. smaller values of k) when computing the full covariance matrix has a negligible effect on the derived constraints. Additionally, for the constraints given in this section we smooth the local velocity field with a gridding scale of $20\,h^{-1}$ Mpc.

The constraints for the parameters are shown in Fig. 12 and the best-fitting values and 68 per cent confidence regions are given in Table 1. Using only the 6dFGSv sample, we determine $\Omega_{\rm m} = 0.136^{+0.07}_{-0.04}$ and $\sigma_8 = 0.69^{+0.18}_{-0.14}$, and for the SNe velocity sample we determine $\Omega_{\rm m} = 0.233^{+0.134}_{-0.09}$ and $\sigma_8 = 0.86 \pm 0.18$. The results show that the two PV samples are consistent with each other and given the size of the errors we do not find a strong statistical tension (less than 2σ) with the parameter values reported by *Planck*. Combining the two PV surveys we determine $\Omega_{\rm m} = 0.166^{+0.11}_{-0.06}$ and $\sigma_8 = 0.74 \pm 0.16$; similarly we find no strong statistical tension with *Planck*. For the matrix hyperparameter analysis, we find $\alpha_{\rm 6dF} = 1.23 \pm 0.05$, $\alpha_{\rm SNe} = 0.87 \pm 0.08$, $\Omega_{\rm m} = 0.228^{+0.12}_{-0.08}$ and $\sigma_8 = 0.96^{+0.14}_{-0.16}$; although the constraints from the hyperparameters are best fitted with the slightly higher σ_8 value, we find the results from the hyperparameter analysis are statistically consistent with the previous constraints, as shown in Fig. 12.

The constraints on $\Omega_{\rm m}$ and σ_8 outlined in this section, while not competitive in terms of statistical uncertainty to other cosmological probes, do offer some insight. In contrast to most methods to determine the matter density, $\Omega_{\rm m}$, constraints from PV do not result from determining properties of the global statistically homogeneous universe (geometric probes); the constraints arise from the dependence of the clustering properties of dark matter on $\Omega_{\rm m}$. The consistency between these probes is a strong test of the cosmological model.

5.3 Velocity power spectrum

Analysing the surveys individually, we consider the base parameter set [$A_1(k_1)$, $A_2(k_2)$, $A_3(k_3)$, $A_4(k_4)$, $A_5(k_5)$, $\sigma_{\rm v}$]. Each A_i parameter (defined in equation 24) acts to scale the amplitude of the velocity power spectrum, $\mathcal{P}_{vv}(k)$, over a specified wavenumber range given by $k_1 \equiv [0.005, 0.02]$, $k_2 \equiv [0.02, 0.05]$, $k_3 \equiv [0.05, 0.08]$, $k_4 \equiv [0.08, 0.12]$ and $k_5 \equiv [0.12, 0.150]$. When combining samples we consider the parameter sets [A_1, A_2, A_3, A_4, A_5, $\sigma_{v,1}$, $\sigma_{v,2}$] and [A_1, A_2, A_3, A_4, A_5, $\alpha_{\rm 6dF}$, $\alpha_{\rm SNe}$]. We use a flat prior on the amplitude parameters, $A_i = [0, 100]$, and the hyperparameters $\alpha_i = [0, 10]$.

The constraints for the amplitude of the velocity power spectrum are shown in Fig. 13 and the best-fitting values and 68 per cent confidence regions are given in Table 2. The deviation between the ML values and median values (as shown in Table 2) is caused by the skewness of the distributions and the physical requirement that $A_i > 0$. This requirement results in a cut-off to the probability distribution that becomes more significant as the size of the errors increases. Therefore, we caution that defining a single best-fitting value from the distribution requires subjective choices; note this is *not* the case for the growth rate constraints as shown in the next section. The fiducial power in each Fourier bin is consistent with that expected in our fiducial cosmological model assuming the best-fitting *Planck* parameters.

5.4 Scale-dependent growth rate

We consider the results outlined in this section the most significant component of this work. We present the first measurement of a scale-dependent growth rate which includes the largest scale growth rate measurement to date (viz. length-scales greater than $300\,h^{-1}$ Mpc). Additionally, we present a redshift zero measurement of the growth rate that is *independent* of galaxy bias and accurate to ∼15 per cent. Comparing this result to that obtained from the RSD measurement of 6dFGS (i.e. Beutler et al. 2012a) allows one to test the systematic

[17] No internal orthogonalization of parameters is required.

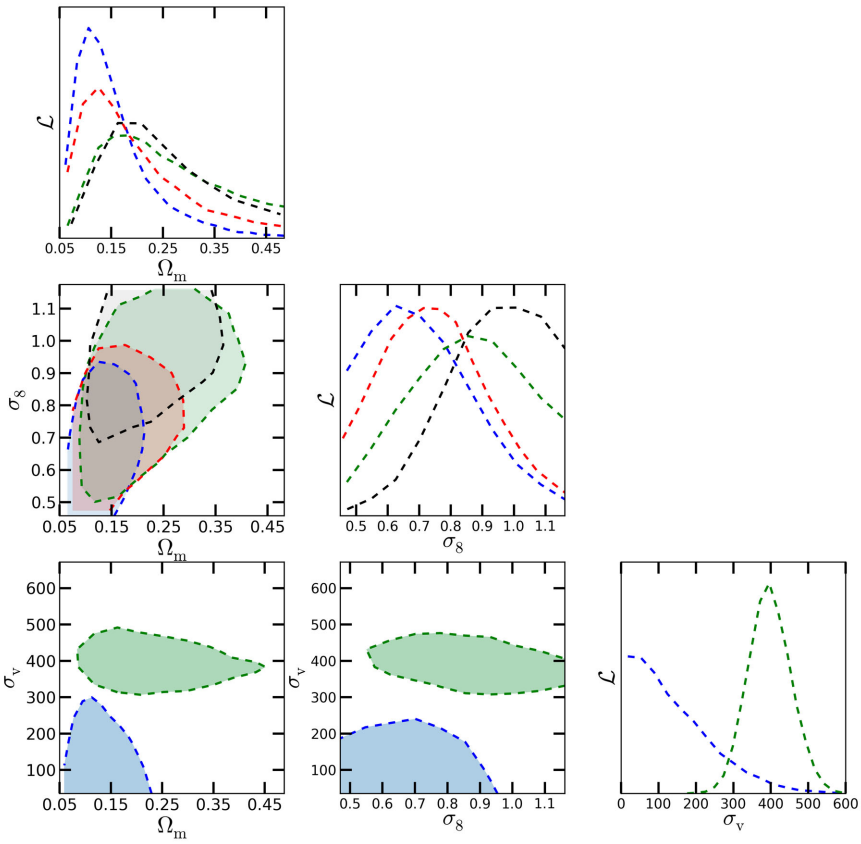

Figure 12. 68 per cent confidence intervals for the matter density Ω_m, σ_8 and the non-linear velocity dispersion σ_v. Results are shown for 6dFGSv (blue), the SN sample (green), the combined analysis (red) and the combined hyperparameter analysis (black). The σ_v constraints from the combined analysis are very similar to the individual constraints hence we do not add them here.

Table 1. Derived cosmological parameter values for Ω_m and σ_8 plus the derived value for the non-linear velocity dispersion σ_v and the hyperparameters α_{6dF} and α_{SNe}. Parameters not allowed to vary are fixed at their *Planck* ML values. Columns 2 and 3 give results from the 6dFGSv survey data alone. Columns 4 and 5 give results from the SNe sample data alone. For columns 6 and 7 we give the results combining both surveys; and for columns 8 and 9 we give the results combining both surveys using a matrix hyperparameter analysis. Note that the hyperparameters are only given for columns 8 and 9 as they are not included in the other analysis. All varied parameters are given flat priors.

Parameter	6dFGSv		SNe		6dFGSv + SNe (Norm)		6dFGSv + SNe (Hyp)	
	ML	Median (68 per cent limits)	ML	Median (68 per cent limits)	ML	Median (68 per cent limits)	ML	Median (68 per cent limits)
Ω_m	0.103	$0.136^{+0.07}_{-0.04}$	0.169	$0.233^{+0.134}_{-0.09}$	0.107	$0.166^{+0.11}_{-0.06}$	0.183	$0.228^{+0.12}_{-0.08}$
σ_8	0.66	$0.69^{+0.18}_{-0.14}$	0.89	0.86 ± 0.18	0.73	0.74 ± 0.16	1.06	$0.96^{+0.14}_{-0.16}$
σ_v[km s^{-1}]	32.7	114^{+245}	388	395^{+54}_{-58}	–	–	–	–
α_{6dF}	–	–	–	–	–	–	1.22	1.23 ± 0.05
α_{SNe}	–	–	–	–	–	–	0.86	0.87 ± 0.08

influence of galaxy bias, a significant source of potential systematic error in RSD analysis.

Analysing the surveys individually we consider two parameter sets: first, we determine the growth rate in the scale-dependent bins defined above constraining the parameter set $[f\sigma_8(k_i), \sigma_v]$ $(i = 1..5)$; secondly, we fit for a single growth rate measurement $[f\sigma_8(z = 0), \sigma_v]$. When combining data sets we consider the extensions to the base parameter set $+[\sigma_{v,1}, \sigma_{v,2}]$ and $+[\alpha_{6dF}, \alpha_{SNe}]$, and use a smoothing length of $10\,h^{-1}$ Mpc. We fix the shape of the fiducial velocity power spectrum Ω_m to the *Planck* value. By separating the power spectrum into wavenumber bins we expect that our final constraints are relatively insensitive to our choice of Ω_m. Varying Ω_m generates a k-dependent variation in the power spectrum over very large scales; considering small intervals of the power spectrum this k-dependence is insignificant and to first order the correction to a variation in Ω_m is simply a change in amplitude of the power spectrum, which we allow to vary in our analysis.

We first consider the scale-dependent constraints which are shown in Fig. 14; with the best fit and 68 per cent confidence internals given in Table 3 and the full probability distributions in Fig. 15. For 6dFGSv we determine: $f\sigma_8(k_i) = [0.72^{+0.17}_{-0.23}, 0.38^{+0.17}_{-0.20}, 0.43^{+0.20}_{-0.20}, 0.55^{+0.22}_{-0.23}, 0.52^{+0.25}_{-0.22}]$. For the SNe velocity

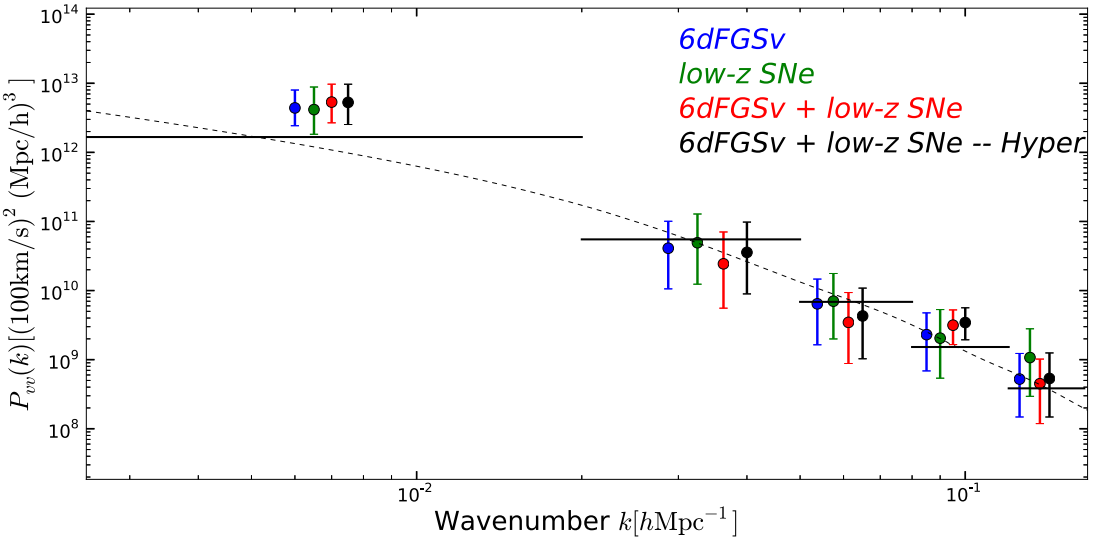

Figure 13. 68 per cent confidence intervals for the amplitude parameters A_i scaled by the mean power within each bin for the 6dFGSv data, SNe data and the combined constraint. The thick blue lines give the mean power in each bin in the fiducial cosmology calculated using equation (26). The black dashed line shows the velocity power spectrum $\mathcal{P}_{vv}(k)$ calculated assuming the *Planck* cosmology. The circle symbols here give the median of the posterior distribution.

Table 2. Constraints on the velocity power spectrum amplitude parameters A_i plus the value of the non-linear velocity dispersion σ_v and the hyperparameters α_{6dF} and α_{SNe}. Parameters not allowed to vary are fixed at their *Planck* ML values. Columns 2 and 3 give results from the 6dFGSv survey data alone. Columns 4 and 5 give results from the SNe sample data alone. For columns 6 and 7 we give the results combining both surveys; and for columns 8 and 9 we give the results combining both surveys using a matrix hyperparameter analysis. All varied parameters are given flat priors.

Parameter	6dFGSv		SNe		6dFGSv + SNe (Norm)		6dFGS + SNe (Hyp)	
	ML	Median (68 per cent limits)	ML	Median (68 per cent limits)	ML	Median (68 per cent limits)	ML	Median (68 per cent limits)
$A_1(k_1)$	1.98	$2.64^{+2.15}_{-1.18}$	1.62	$2.50^{+2.80}_{-1.40}$	2.43	$3.20^{+2.62}_{-1.60}$	2.22	$3.17^{+2.64}_{-1.65}$
$A_2(k_2)$	0.20	$0.74^{+1.08}_{-0.55}$	0.25	$0.89^{+1.43}_{-0.67}$	0.14	$0.44^{+0.84}_{-0.34}$	0.26	$0.65^{+1.13}_{-0.49}$
$A_3(k_3)$	0.20	$0.94^{+1.20}_{-0.70}$	0.57	$1.0^{+1.55}_{-0.73}$	0.13	$0.50^{+0.86}_{-0.38}$	0.27	$0.63^{+0.96}_{-0.48}$
$A_4(k_4)$	0.27	$1.51^{+1.61}_{-1.06}$	0.43	$1.34^{+2.14}_{-0.99}$	1.52	$2.07^{+1.37}_{-0.98}$	1.89	$2.26^{+1.43}_{-0.99}$
$A_5(k_5)$	0.30	$1.36^{+1.84}_{-0.98}$	0.84	$2.79^{+4.49}_{-2.03}$	0.38	$1.17^{+1.48}_{-0.86}$	0.40	$1.39^{+1.86}_{-1.00}$
$\sigma_v[\mathrm{km\ s^{-1}}]$	98.4	137.5^{+110}_{-91}	372.8	365.2^{+43}_{-45}	–	–	–	–
α_{6dF}	–	–	–	–	–	–	1.198	1.189 ± 0.034
α_{SNe}	–	–	–	–	–	–	0.940	$0.980^{+0.104}_{-0.091}$

sample we have: $f\sigma_8(k_i) = [0.70^{+0.29}_{-0.22}, 0.42^{+0.23}_{-0.19}, 0.45^{+0.24}_{-0.20}, 0.51^{+0.29}_{-0.23}, 0.74^{+0.41}_{-0.33}]$. As shown in Table 3 the constraints on σ_v from 6dFGSv are very weak relative to the constraints from the SNe sample. The reason the σ_v parameter is much lower (and has a larger uncertainty) for the 6dFGSv sample relative to the SNe sample is that the gridding has a stronger effect for the 6dFGSv sample given the higher number density. This significantly reduces the contribution of non-linear velocity dispersion to the likelihood and hence increases the final uncertainty. In addition, we note that the magnitude of σ_v will be dependent on the mass of the dark matter halo that the galaxy resides in. The halo mass may vary between PV surveys, therefore, causing σ_v to vary between PV surveys.

The results (again) show that the two surveys are consistent with each other, viz. they are within one standard deviation of each other for all growth rate measurements. We detect no significant fluctuations from a scale-independent growth rate as predicted by the standard ΛCDM cosmological model. Although the power in the largest scale Fourier bin is high, it is consistent with statistical fluctuations. When combining both the 6dFGSv sample and the SNe velocity sample we find (no hyperparameters): $f\sigma_8(k_i) = [0.79^{+0.21}_{-0.25}, 0.30^{+0.14}_{-0.19}, 0.32^{+0.19}_{-0.15}, 0.64^{+0.17}_{-0.16}, 0.48^{+0.22}_{-0.21}]$. We find no significant departure from the predictions of the standard model.

We next fit for a scale-independent growth rate by scaling the fiducial power spectrum across the full wavenumber range. The measurements of a scale-independent growth rate of structure are given in Fig. 16. Here we also compare with previously published results from RSD measurements and the predictions from the assumed fiducial cosmology. The best-fitting values and 68 per cent confidence intervals are given at the bottom of Table 3. We also plot the full probability distributions in Fig. 17, in addition to the results from the hyperparameter analysis. For 6dFGSv, the SNe velocity sample and 6dFGSv+ SNe (with no hyperparameters) we determine, respectively, $f\sigma_8(z) = [0.428^{+0.079}_{-0.068}, 0.417^{+0.097}_{-0.084}, 0.418 \pm 0.065]$. The measurements of the growth rate all show consistency with the predictions from the fiducial model as determined by *Planck*. Specifically, the best-fitting

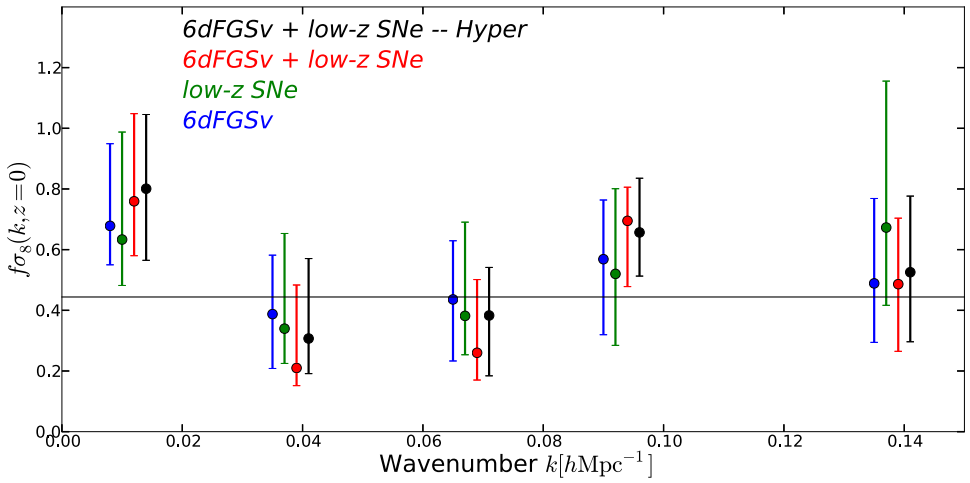

Figure 14. 68 per cent confidence intervals for the normalized *scale-dependent* growth rate $f(z=0,k)\sigma(z=0)$ in five different bins in Fourier space. The thick black line is the prediction found assuming the fiducial *Planck* cosmology. For each k-bin, we plot the results from 6dFGSv, the SNe sample and the combined constraint. The bin intervals used here are given in Section 5.3. The largest scale bin corresponds to length-scales $>300\,h^{-1}$ Mpc. The circle symbols give the ML of the posterior distribution.

Table 3. Constraints on the growth rate as a function of scale and independent of scale (final row) plus the value of the non-linear velocity dispersion σ_v and the hyperparameters α_{6dF} and α_{SNe}. Columns 2 and 3 give results from the 6dFGSv survey data alone. Columns 4 and 5 give results from the SNe sample data alone. For columns 6 and 7, we give the results combining both surveys, and for columns 8 and 9 we give the results combining both surveys using a matrix hyperparameter analysis.

Parameter	6dFGSv		SNe		6dFGSv + SNe (Norm)		6dFGS + SNe (Hyp)	
	ML	Median (68 per cent limits)	ML	Median (68 per cent limits)	ML	Median (68 per cent limits)	ML	Median (68 per cent limits)
$f\sigma_8(k_1)$	0.68	$0.72^{+0.17}_{-0.23}$	0.63	$0.70^{+0.29}_{-0.22}$	0.76	$0.79^{+0.21}_{-0.25}$	0.79	$0.80^{+0.23}_{-0.25}$
$f\sigma_8(k_2)$	0.39	$0.38^{+0.17}_{-0.20}$	0.34	$0.42^{+0.23}_{-0.19}$	0.21	$0.30^{+0.14}_{-0.19}$	0.31	$0.36^{+0.17}_{-0.21}$
$f\sigma_8(k_3)$	0.44	$0.43^{+0.20}_{-0.20}$	0.38	$0.45^{+0.24}_{-0.20}$	0.260	$0.32^{+0.19}_{-0.15}$	0.38	$0.35^{+0.17}_{-0.19}$
$f\sigma_8(k_4)$	0.57	$0.55^{+0.22}_{-0.23}$	0.52	$0.51^{+0.29}_{-0.23}$	0.69	$0.64^{+0.17}_{-0.16}$	0.66	$0.66^{+0.17}_{-0.19}$
$f\sigma_8(k_5)$	0.49	$0.52^{+0.25}_{-0.22}$	0.67	$0.74^{+0.41}_{-0.33}$	0.49	$0.48^{+0.22}_{-0.21}$	0.53	$0.52^{+0.15}_{-0.17}$
σ_v [km s^{-1}]	98.4	137.5^{+110}_{-91}	372.8	365.2^{+43}_{-45}	–	–	98.4	372.8
α_{6dF}	–	–	–	–	–	–	1.198	1.189 ± 0.034
α_{SNe}	–	–	–	–	–	–	0.940	$0.980^{+0.104}_{-0.091}$
$f\sigma_8(z=0)$	0.424	$0.428^{+0.079}_{-0.068}$	0.432	$0.417^{+0.097}_{-0.084}$	0.429	0.418 ± 0.065	0.492	$0.496^{+0.044}_{-0.108}$

Planck parameters predict $f\sigma_8(z=0)=0.443$. In addition, we find consistency with the measurement of the growth rate of structure from the RSD analysis of the 6dFGS (see Fig. 16) (Beutler et al. 2012a).

For the hyperparameter analysis, the results for the scale-dependent and scale-independent measurements are indistinguishable. We determine $\alpha_{6dF}=1.189\pm0.034$ and $\alpha_{SNe}=0.980^{+0.104}_{-0.091}$; the results for both analysis have been included in Figs 14 and 16. We find that, while there is a slight shift in the best-fitting values, the hyperparameter analysis gives results statistically consistent with the previous results; for the scale-independent measurements this is best shown in Fig. 17.

6 DISCUSSION AND CONCLUSIONS

We have constructed 2-point statistics of the velocity field and tested the ΛCDM cosmology by using low-redshift 6dFGSv and Type Ia SNe data. We summarize our results as follows.

(i) We introduced and tested a new method to constrain the scale-dependence of the normalized growth rate using only PV data. Using this method, we present the *largest scale* constraint on the growth rate of structure to date. For length-scales greater than $\sim300\,h^{-1}$ Mpc ($k<0.02\,h\,\mathrm{Mpc}^{-1}$) we constrain the growth rate to ∼30 per cent. Specifically, we find for 6dFGSv, which provides our best constraints, $f\sigma_8(k<0.02\,h\,\mathrm{Mpc}^{-1})=0.72^{+0.17}_{-0.23}$. This result is consistent with the standard model prediction of $f\sigma_8(z=0)=0.4439$, albeit higher than expected.

(ii) Examining the scale-dependence of the growth rate of structure at $z=0$, we find the constraints $f\sigma_8(k_i)=[0.79^{+0.21}_{-0.25}, 0.30^{+0.14}_{-0.19}, 0.32^{+0.19}_{-0.15}, 0.64^{+0.17}_{-0.16}, 0.48^{+0.22}_{-0.21}]$ using the wavenumber ranges $k_1\equiv[0.005,\ 0.02]$, $k_2\equiv[0.02,\ 0.05]$, $k_3\equiv[0.05,\ 0.08]$, $k_4\equiv[0.08,\ 0.12]$ and $k_5\equiv[0.12,\ 0.150]$. We find no evidence for a scale-dependence in the growth rate, which is consistent with the standard model. All the growth rate measurements are consistent with the fiducial *Planck* cosmology.

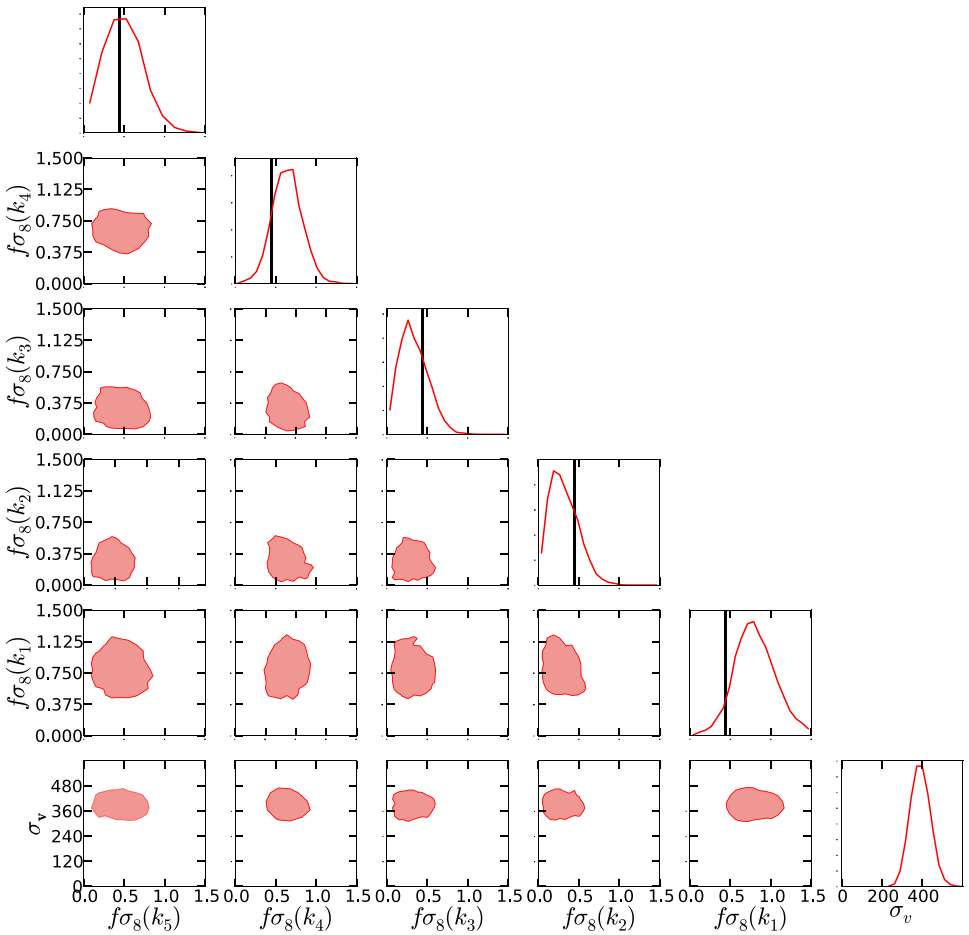

Figure 15. 68 per cent confidence intervals for the normalized growth rate $f(k, z = 0)\sigma(z = 0)$ for the combined constraints (using no hyperparameters). The prediction for the growth rate of structure assuming a fiducial *Planck* cosmology is given by the solid black line.

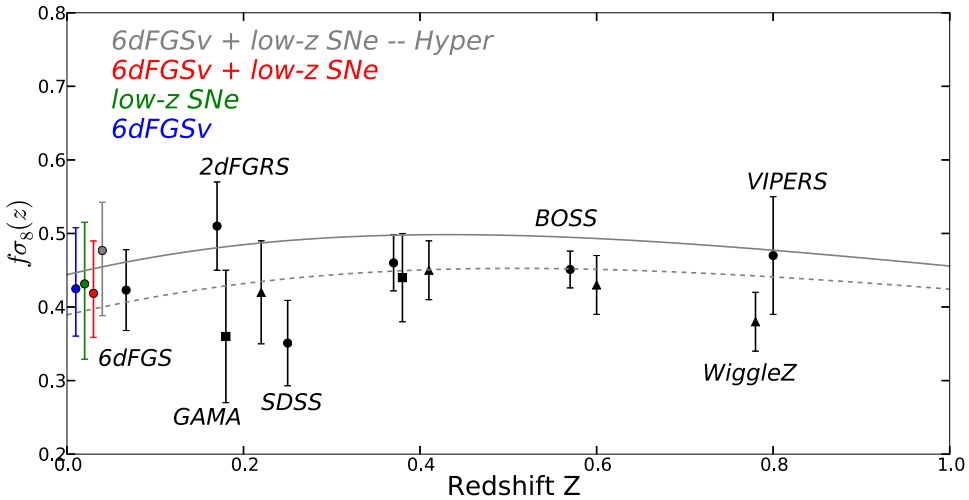

Figure 16. 68 per cent confidence intervals for the normalized growth rate $f(z = 0)\sigma(z = 0)$ averaging over all scales. The solid black line gives the theoretical prediction for $f\sigma_8(z)$ assuming the *Planck* cosmology and the dashed-black line gives the prediction assuming the *Wilkinson Microwave Anisotropy Probe* cosmology. The redshift separation of the PV measurements (coloured points) is simply to avoid overlapping data points; the redshift of the green data point gives the redshift of all the points. We compare our PV measurements to previous constraints from RSD measurements from the 6dFGS, 2dFGRS, GAMA, WiggleZ, SDSS LRG, BOSS CMASS and VIPERS surveys given by the black points (Hawkins et al. 2003; Blake et al. 2011a, 2013; Beutler et al. 2012a; de la Torre et al. 2013; Samushia et al. 2013).

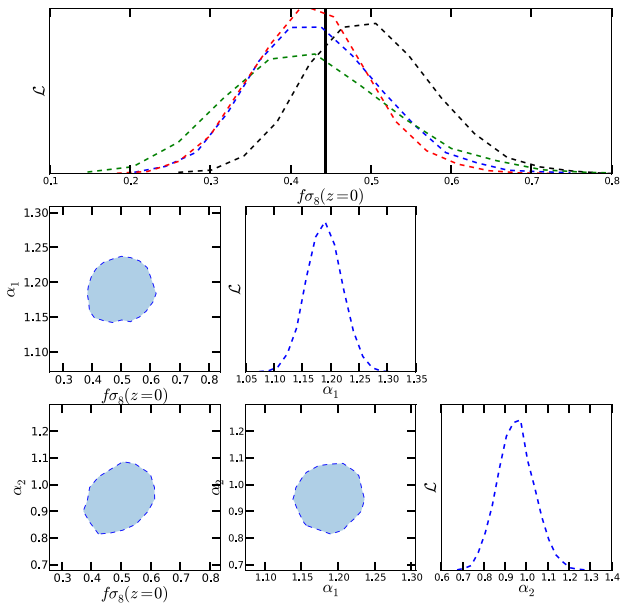

Figure 17. Posterior distributions for the (scale averaged) growth rate of structure $f\sigma_8(z=0)$ for 6dFGSv (blue), SNe (green), combining samples (red) and for the hyperparameter analysis (black). The posterior distributions are also given for the hyperparameters $\alpha_{\rm 6dF}$ and $\alpha_{\rm SNe}$. The prediction for the growth rate of structure assuming a fiducial *Planck* cosmology is given by the solid black line.

(iii) Averaging over all scales, we measure the growth rate to ∼15 per cent which is *independent* of galaxy bias. This result $f\sigma_8(z=0)=0.418\pm0.065$ is consistent with the RSD analysis of 6dFGS which produced a measurement of $f\sigma_8(z)=0.423\pm0.055$ (Beutler et al. 2012a), increasing our confidence in the modelling of galaxy bias. In addition, this measurement is consistent with the constraint given by Hudson & Turnbull (2012) of $f\sigma_8=0.400\pm0.07$, found by comparing the local velocity and density fields. In contrast to our constraint this measurement is sensitive to galaxy bias and any systematic errors introduced during velocity field reconstruction.

(iv) We also consider various other methods to constrain the standard model. We directly constrain the amplitude of the velocity power spectrum $\mathcal{P}_{vv}(k)\equiv\mathcal{P}_{\theta\theta}(k)/k^2$ for the same scale range as specified above; we find that the predictions from two loop multi-point propagators assuming the *Planck* cosmology gives an accurate description of the measured velocity power spectrum. Specifically, the derived amplitudes A_i of the power spectrum of four bins are consistent with the fiducial cosmology at the 1σ level, and the largest scale bin is consistent at the 2σ level. We can also compare these constraints to those given by Macaulay et al. (2012). Similarly to our results they found the amplitude of the matter power spectrum, determined using the composite sample of PVs, to be statistically consistent with the standard ΛCDM cosmology. In addition, they also find on the largest scales a slightly higher amplitude of the power spectrum that is expected in the standard model.[18]

(v) We show that when analysing PV surveys with velocities derived using the FP or the Tully–Fisher relation, one should perform the analysis using a variable that is a linear transformation of $x=\log_{10}(D_z/D_{\rm H})$. We show the intrinsic scatter is not Gaussian for the PV and this can significantly bias cosmological constraints. We show how the analysis can be reformulated using the variable δm, which removes the bias.

With a large number of upcoming PV surveys, the prospect for understanding how structure grows in the low-redshift universe is excellent. Future work will move beyond consistency tests by adopting specific modified gravity models and phenomenological parametrizations, including measurements of RSDs and by self-consistently modifying the growth and evolutionary history of the universe. This will allow a vast range of spatial and temporal scales to be probed simultaneously, providing a strong and unique test of the standard ΛCDM model, and perhaps even providing some insight on the so-far mysterious dark energy component of the universe.

[18] Note we cannot directly compare these sets of results, given different bin ranges were used.

ACKNOWLEDGEMENTS

We are grateful for a very constructive referee report from Andrew Jaffe. AJ, JK and CMS are supported by the Australian Research Council Centre of Excellence for All-Sky Astrophysics (CAASTRO) through project number CE110001020. CB acknowledges the support of the Australian Research Council through the award of a Future Fellowship. TMD acknowledges the support of the Australian Research Council through a Future Fellowship award, FT100100595. This work was performed on the gSTAR national facility at Swinburne University of Technology. gSTAR is funded by Swinburne and the Australian Governments Education Investment Fund.

REFERENCES

Abate A., Erdoğdu P., 2009, MNRAS, 400, 1541
Abate A., Bridle S., Teodoro L. F. A., Warren M. S., Hendry M., 2008, MNRAS, 389, 1739
Anderson L. et al., 2013, MNRAS, 439, 83
Armendariz-Picon C., Mukhanov V., Steinhardt P. J., 2000, Phys. Rev. Lett., 85, 4438
Bean R., Tangmatitham M., 2010, Phys. Rev. D, 81, 083534
Bernardeau F., Crocce M., Scoccimarro R., 2008, Phys. Rev. D, 78, 103521
Bernardi M. et al., 2003, AJ, 125, 1817
Beutler F. et al., 2012a, MNRAS, 423, 3430
Beutler F. et al., 2013b, preprint (arXiv:e-prints)
Blake C. et al., 2011a, MNRAS, 415, 2876
Blake C. et al., 2011b, MNRAS, 415, 2892
Blake C. et al., 2013, MNRAS, 436, 3089
Bonvin C., Durrer R., Gasparini M. A., 2006, Phys. Rev. D, 73, 023523
Bridle S. L., Crittenden R., Melchiorri A., Hobson M. P., Kneissl R., Lasenby A. N., 2002, MNRAS, 335, 1193
Caldwell R. R., Dave R., Steinhardt P. J., 1998, Phys. Rev. Lett., 80, 1582
Campbell L. et al., 2014, MNRAS, 443, 1231
Clifton T., 2013, Int. J. Mod. Phys. D, 22, 30004
Clifton T., Ferreira P. G., Padilla A., Skordis C., 2012, Phys. Rep., 513, 1
Cole S., Kaiser N., 1989, MNRAS, 237, 1127
Colless M., Saglia R. P., Burstein D., Davies R. L., McMahan R. K., Wegner G., 2001, MNRAS, 321, 277
Colless M., Beutler F., Blake C., 2013, in de Grijs R., ed., Proc. IAU Symp. 289, Advancing the Physics of Cosmic Distances. Cambridge Univ. Press, Cambridge, p. 319
Conley A. et al., 2011, ApJS, 192, 1
Cresswell J. G., Percival W. J., 2009, MNRAS, 392, 682
Crocce M., Scoccimarro R., 2006, Phys. Rev. D, 73, 063519
Crocce M., Scoccimarro R., Bernardeau F., 2012, MNRAS, 427, 2537
Daniel S. F., Linder E. V., 2013, J. Cosmol. Astropart. Phys., 2, 7
Davis T. M. et al., 2011, ApJ, 741, 67

de la Torre S. et al., 2013, A&A, 557, A54
Desjacques V., Crocce M., Scoccimarro R., Sheth R. K., 2010, Phys. Rev. D, 82, 103529
Dodelson S., 2003, Modern Cosmology. Academic Press, New York
Folatelli G. et al., 2010, AJ, 139, 120
Foreman-Mackey D., Hogg D. W., Lang D., Goodman J., 2013, PASP, 125, 306
Freedman W. L., Madore B. F., Scowcroft V., Burns C., Monson A., Persson S. E., Seibert M., Rigby J., 2012, ApJ, 758, 24
Freudling W. et al., 1999, ApJ, 523, 1
Fry J. N., Gaztanaga E., 1993, ApJ, 413, 447
Ganeshalingam M., Li W., Filippenko A. V., 2013, MNRAS, 433, 2240
Goodman J., Weare J., 2010, Commun. Appl. Math. Comput. Sci., 5, 65
Gordon C., Land K., Slosar A., 2007, Phys. Rev. Lett., 99, 081301
Hawkins E. et al., 2003, MNRAS, 346, 78
Hicken M., Wood-Vasey W. M., Blondin S., Challis P., Jha S., Kelly P. L., Rest A., Kirshner R. P., 2009, ApJ, 700, 1097
Hobson M. P., Bridle S. L., Lahav O., 2002, MNRAS, 335, 377
Hu W., Scranton R., 2004, Phys. Rev. D, 70, 123002
Hudson M. J., Turnbull S. J., 2012, ApJ, 751, L30
Hui L., Greene P. B., 2006, Phys. Rev. D, 73, 123526
Jaffe A. H., Kaiser N., 1995, ApJ, 455, 26
Jarrett T. H., Chester T., Cutri R., Schneider S., Skrutskie M., Huchra J. P., 2000, AJ, 119, 2498
Jennings E., Baugh C. M., Pascoli S., 2011, MNRAS, 410, 2081
Jennings E., Baugh C. M., Li B., Zhao G.-B., Koyama K., 2012, MNRAS, 425, 2128
Jones D. H. et al., 2004, MNRAS, 355, 747
Jones D. H., Peterson B. A., Colless M., Saunders W., 2006, MNRAS, 369, 25
Jones D. H. et al., 2009, MNRAS, 399, 683
Kaiser N., 1988, MNRAS, 231, 149
Kessler R. et al., 2009, ApJS, 185, 32
Kowalski M. et al., 2008, ApJ, 686, 749
Lahav O., Bridle S. L., Hobson M. P., Lasenby A. N., Sodré L., 2000, MNRAS, 315, L45
Lewis A., Challinor A., Lasenby A., 2000, ApJ, 538, 473
Linder E. V., 2005, Phys. Rev. D, 72, 043529
Linder E. V., 2013, J. Cosmol. Astropart. Phys., 4, 31
Lombriser L., Schmidt F., Baldauf T., Mandelbaum R., Seljak U., Smith R. E., 2012, Phys. Rev. D, 85, 102001
Macaulay E., Feldman H. A., Ferreira P. G., Jaffe A. H., Agarwal S., Hudson M. J., Watkins R., 2012, MNRAS, 425, 1709
Magoulas C., Colless M., Jones D., Springob C., Mould J., 2010, in Bruzual G. R., Charlot S., eds, Proc. IAU Symp. 262, Stellar Populations – Planning for the Next Decade. Cambridge Univ. Press, Cambridge, p. 376
Magoulas C. et al., 2012, MNRAS, 427, 245
Ma Y.-Z., Berndsen A., 2013, Astron. Comput., 5, 45
Ma Y.-Z., Scott D., 2013, MNRAS, 428, 2017
Ma Y.-Z., Gordon C., Feldman H. A., 2011, Phys. Rev. D, 83, 103002
Ma Y.-Z., Taylor J. E., Scott D., 2013, MNRAS, 436, 2029
Parfrey K., Hui L., Sheth R. K., 2011, Phys. Rev. D, 83, 063511
Peebles P. J. E., 1993, Principles of Physical Cosmology. Princeton Univ. Press, Princeton
Planck Collaboration XVI, 2013, preprint (arXiv:1303.5076)
Poole G. B. et al., 2014, preprint (arXiv:1407.0390)
Pyne T., Birkinshaw M., 2004, MNRAS, 348, 581
Reid B. A. et al., 2012, MNRAS, 426, 2719
Samushia L. et al., 2013, MNRAS, 429, 1514
Saulder C., Mieske S., Zeilinger W. W., Chilingarian I., 2013, A&A, 557, A21
Scoccimarro R., 2004, Phys. Rev. D, 70, 083007
Silberman L., Dekel A., Eldar A., Zehavi I., 2001, ApJ, 557, 102
Sotiriou T. P., Faraoni V., 2010, Rev. Mod. Phys., 82, 451
Springel V., 2005, MNRAS, 364, 1105
Springel V., White S. D. M., Tormen G., Kauffmann G., 2001, MNRAS, 328, 726
Springob C. M., Masters K. L., Haynes M. P., Giovanelli R., Marinoni C., 2007, ApJS, 172, 599
Strauss M. A., Willick J. A., 1995, Phys. Rep., 261, 271
Tonry J. L. et al., 2003, ApJ, 594, 1
Tsujikawa S., 2010, in Wolschin G., ed., Lecture Notes in Physics, Vol. 800, Lectures on Cosmology Accelerated Expansion of the Universe. Springer-Verlag, Berlin, p. 99
Turnbull S. J., Hudson M. J., Feldman H. A., Hicken M., Kirshner R. P., Watkins R., 2012, MNRAS, 420, 447
Watkins R., Feldman H. A., Hudson M. J., 2009, MNRAS, 392, 743
Wiltshire D. L., 2013, preprint (arXiv:1311.3787)
Wiltshire D. L., Smale P. R., Mattsson T., Watkins R., 2013, Phys. Rev. D, 88, 083529
Zaroubi S., Bernardi M., da Costa L. N., Hoffman Y., Alonso M. V., Wegner G., Willmer C. N. A., Pellegrini P. S., 2001, MNRAS, 326, 375
Zehavi I., Dekel A., 2000, in Courteau S., Willick J., eds, ASP Conf. Ser. Vol. 201, Cosmological Parameters and Power Spectrum from Peculiar Velocities. Astron. Soc. Pac., San Francisco, p. 262

[1]*Centre for Astrophysics & Supercomputing, Swinburne University of Technology, P.O. Box 218, Hawthorn, VIC 3122, Australia*
[2]*ARC Centre of Excellence for All-sky Astrophysics (CAASTRO)*
[3]*Canadian Institute for Theoretical Astrophysics, Toronto, Canada*
[4]*Department of Physics and Astronomy, University of British Columbia, Vancouver, BC V6T 1Z1, Canada*
[5]*Research School of Astronomy and Astrophysics, Australian National University, Canberra, ACT 2611, Australia*
[6]*Institut de Ciències de l'Espai, IEEC-CSIC, Campus UAB, Facultat de Ciències, Torre C5 par-2, E-08193 Barcelona, Spain*
[7]*School of Mathematics and Physics, University of Queensland, Brisbane, QLD 4072, Australia*
[8]*School of Physics, Monash University, Clayton, VIC 3800, Australia*
[9]*Australian Astronomical Observatory, P.O. Box 915, North Ryde, NSW 1670, Australia*
[10]*School of Physics, University of Melbourne, Parkville, VIC 3010, Australia*
[11]*Department of Astronomy, University of Cape Town, Private Bag X3, Rondebosch 7701, South Africa*
[12]*Department of Physics, University of Durham, Durham DH1 3LE, UK*
[13]*Department of Physics and Astronomy, University of Waterloo, Waterloo, ON N2L 3G1, Canada*
[14]*Perimeter Institute for Theoretical Physics, 31 Caroline St. N., Waterloo, ON N2L 2Y5, Canada*
[15]*International Centre for Radio Astronomy Research, M468, University of Western Australia, 35 Stirling Hwy, Crawley, WA 6009, Australia*

This paper has been typeset from a TEX/LATEX file prepared by the author.